

# Cancer-Erythrocyte Membrane-Mimicking Fe<sub>3</sub>O<sub>4</sub> Nanoparticles and DHJS for Ferroptosis/Immunotherapy Synergism in Tumors

Kaixu Yu, Ying Chen, Lu Zhang, Yongqiang Zheng, Jinlin Chen, Zhenhua Wang, Xiaogang Yu, Kehan Song, Yimin Dong, Fanxiu Xiong, Zijian Dong, Hao Zhu, Gaohong Sheng, Meipeng Zhu, Xi Yuan, Hanfeng Guan, Jiaqiang Xiong,\* Yi Liu,\* and Feng Li\*



Cite This: <https://doi.org/10.1021/acsami.3c07379>



Read Online

ACCESS |



Metrics & More



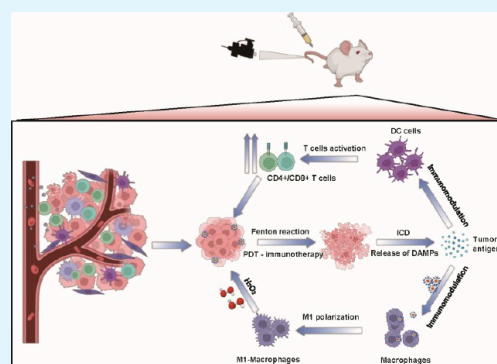
Article Recommendations



Supporting Information

**ABSTRACT:** Ferroptosis is characterized by iron accumulation and lipid peroxidation. However, a clinical dose of Fe<sub>3</sub>O<sub>4</sub> nanoparticles could not cause effective ferroptosis in tumors, and the mechanism is yet to be completely understood. In this study, using RNA-seq data, we found that tumor cells could feedback-activate the antioxidant system by upregulating Nrf-2 expression, thus avoiding ferroptosis caused by Fe<sub>3</sub>O<sub>4</sub> nanoparticles. We also found that DHJS (a probe for ROS generation) can antagonize Nrf-2 expression when it synergizes with Fe<sub>3</sub>O<sub>4</sub> nanoparticles, thus inducing ferroptosis in tumor cells. Considering these findings, we created a biomimetic hybrid cell membrane camouflaged by PLGA-loaded Fe<sub>3</sub>O<sub>4</sub> and DHJS to treat osteosarcoma. The hybrid cell membrane endowed the core nanoparticle with the extension of blood circulation life and enhanced homologous targeting ability. In addition, DHJS and Fe<sub>3</sub>O<sub>4</sub> in nanoparticles prompted synergistically lethal ferroptosis in cancer cells and induced macrophage M1 polarization as well as the infiltration of CD8(+) T cells and dendritic cells in tumors. In summary, this study provides novel mechanistic insights and practical strategies for ferroptosis induction of Fe<sub>3</sub>O<sub>4</sub> nanoparticles. Meanwhile, the synthesized biomimetic nanoparticles exhibited synergistic ferroptosis/immunotherapy against osteosarcoma.

**KEYWORDS:** hybrid membrane, iron oxide nanoparticles, cancer therapy, synergistic ferroptosis/immunomodulation, DNA repair



## INTRODUCTION

Osteosarcoma is the most common and aggressive primary bone malignancy that occurs mostly in young adults and adolescents.<sup>1</sup> The development of osteosarcoma treatment has stagnated over the past 30 years because of its high multidrug resistance (MDR) and immunosuppressive microenvironment,<sup>2,3</sup> and the traditional combination of chemotherapy and surgery regimens has failed to improve the long-term survival of osteosarcoma patients.<sup>4,5</sup> The rising burden of cancer requires novel efficacious treatment modalities. Ferroptosis, as a novel form of programmed cell death, is characterized by iron overload, accumulation of reactive oxygen species (ROS), and lipid peroxidation (LPO); it is morphologically, genetically, and biochemically distinct from necrosis, apoptosis, and autophagy.<sup>6,7</sup> Inducing ferroptosis has become a potential strategy for cancer treatment, which can potentially overcome resistance to tumor therapy and immune escape mechanisms.<sup>8</sup> However, owing to poor pharmacokinetics and organ targeting, as well as the indiscriminate disruption of ferroptosis-related metabolism, the therapeutic effects of recent cancer treatment strategies based on ferroptosis are generally far from satisfactory.<sup>9</sup> To overcome the deficiencies of conventional strategies, there is an urgent unmet need to develop a more desirable therapeutic approach specifically designed for inducing ferroptosis.

In preclinical and clinical settings, iron oxide (Fe<sub>3</sub>O<sub>4</sub>) nanoparticles have been widely used as FDA-approved contrast agents and drug carriers.<sup>10</sup> After Fe<sub>3</sub>O<sub>4</sub> nanoparticles are phagocytosed by cancer cells, they can exert peroxidase-like activity and irreversibly catalyze the Fenton reaction ( $\text{Fe}^{2+} + \text{H}_2\text{O}_2 \rightarrow \text{Fe}^{3+} + \text{HO}\cdot + \text{OH}^-$ ) to generate intracellular ROS and cause potential ferroptosis.<sup>11–13</sup> The burden of intracellular oxidative stress due to a clinical dose of Fe<sub>3</sub>O<sub>4</sub> nanoparticles cannot cause significant cytotoxicity for cancer cells; however, the mechanism by which cancer cells avoid potential ferroptosis has yet to be fully determined. To explore the relationship and the implications of Fe<sub>3</sub>O<sub>4</sub> nanoparticles and potential ferroptosis, we analyzed the RNA-seq and microarray data sets from GEO in this study.<sup>14</sup> We found that cancer cells could feedback-activate the intracellular antioxidant system by upregulating the expression of nuclear factor erythroid-2 related

Received: June 2, 2023

Accepted: August 30, 2023

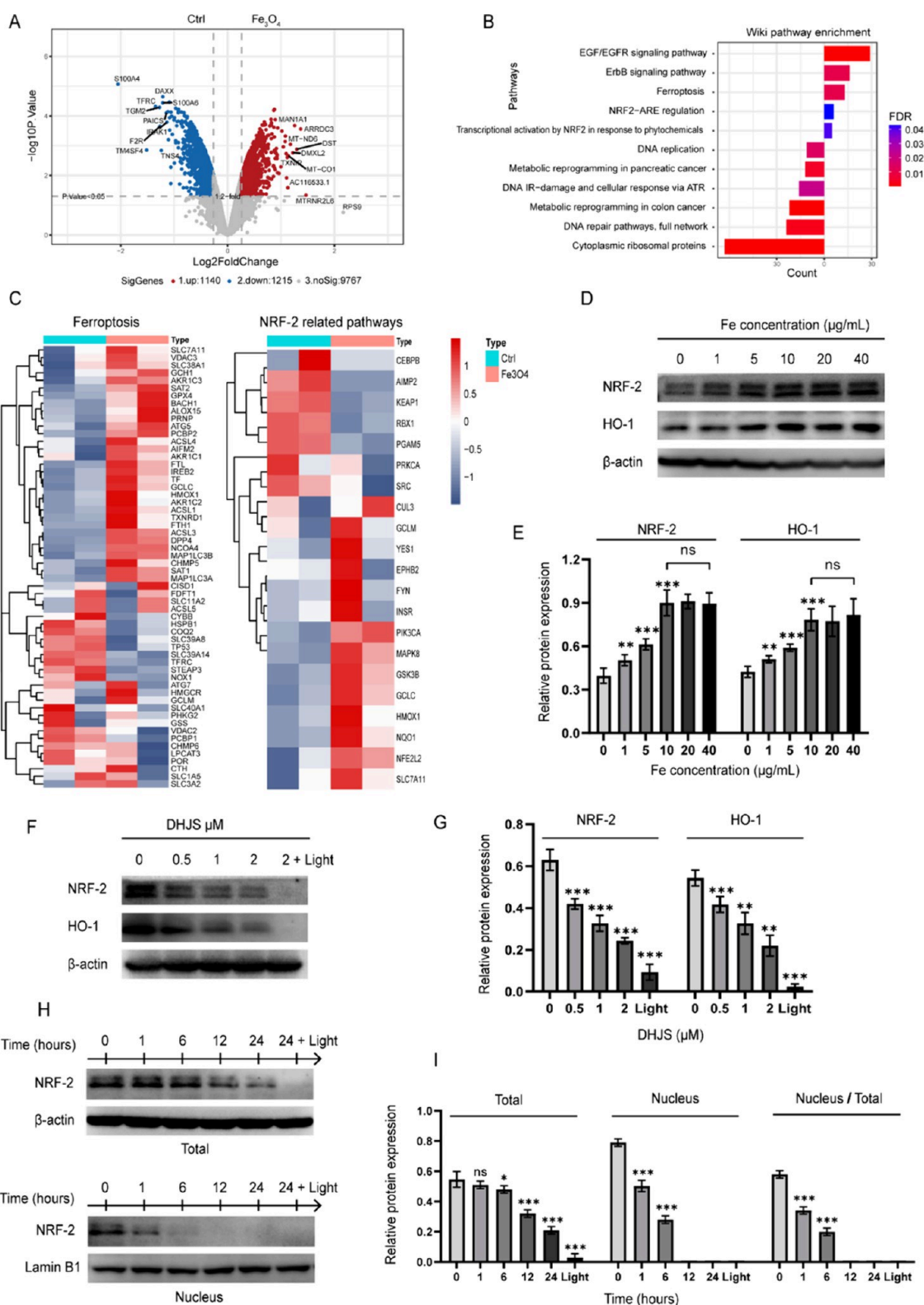


**Figure 1.** Cancer cells can prevent Fe<sub>3</sub>O<sub>4</sub> nanoparticle-induced lethal ferroptosis by overexpressing the Nrf-2 related antioxidant system (A–E). DHJS can inhibit the expression of Nrf-2 and interrupt the signal transduction of Nrf2 in a dose-dependent manner (F–I). (A) Volcano plot of differentially expressed genes (DEGs) in GSE15248. Gene alteration with a fold change greater than 1.2 and an adjusted *p* value <0.05 was identified to be statistically significant. (B) KEGG pathway analyses of overlapping DEGs. (C) Expression heatmap showing the DEGs involved in Nrf2-related and ferroptosis pathways. (D, E) Effect of Fe<sub>3</sub>O<sub>4</sub> nanoparticles on the overall expression of Nrf2-related pathways in HOS cells (*n* = 3). (F, G) Effect of DHJS nanoparticles on the overall expression of Nrf2-related pathways in HOS cells (*n* = 3 and 8.5 mW/cm<sup>2</sup> for 30 min). (H, I) Effect of DHJS on the overall expression and transportation of Nrf2 to the nucleus in HOS cells (*n* = 3 and 8.5 mW/cm<sup>2</sup> for 30 min). Data are presented as mean  $\pm$  SEM and were analyzed using unpaired two-sided Student's *t* test (ns: no significance, \**p* < 0.05, \*\**p* < 0.01, \*\*\**p* < 0.001).

factor 2 (Nrf-2), thus avoiding ferroptosis after treatment with Fe<sub>3</sub>O<sub>4</sub> nanoparticles. Nrf-2, a basic leucine zipper protein, plays an important role in the regulation of antioxidant proteins, such as oxygenase-1 (HO-1) and NAD(P)H quinone dehydrogenase 1 (NQO1), to protect cells against oxidative stress damage.<sup>15</sup>

Our previous research demonstrated that DHJS possessed excellent near-infrared fluorescence imaging ability *in vitro* and *in vivo* even after 24 h, as well as exhibited good photodynamic toxicity (PDT) to cancer cells.<sup>16</sup> In the current study, we found that DHJS alone could significantly inhibit the expression of Nrf-2 in a dose-dependent manner and reverse the activation of Nrf2-related pathways caused by the treatment of Fe<sub>3</sub>O<sub>4</sub> nanoparticles. Therefore, DHJS can potentially synergize with Fe<sub>3</sub>O<sub>4</sub> nanoparticles to induce lethal ferroptosis in cancer cells.

Relative to the traditional approach of chemical-ligand-related surface modification, fused cell membrane-coated nanoparticle (CCNP) technology has been highly regarded and is considered mature.<sup>17–19</sup> This method retains the physicochemical properties of synthetic core nanoparticles as well as endows nanoparticles with extraordinary biointerfacing function, including homologous targeting, immune evasion, and long circulation time.<sup>20–22</sup> Further, the combination of CCNP technology and anticancer immunotherapy has been increasingly applied in nanomedicine.<sup>23–25</sup> Efforts directed toward anticancer immunotherapy in recent decades have also demonstrated that immunogenic cell death (ICD) such as ferroptosis could activate an immune response specific for cancer cells as well as generate a strong and long-lasting anticancer immunity.<sup>26,27</sup> For example, Xu et al. reported on a polymer multicellular nanoengager with a photothermal core camouflaged with fused membranes derived from tumor cells and dendritic cells (DCs) as the cancer vaccine shell to induce ICD and achieve enhanced photothermal immunotherapy.<sup>24</sup>

In the current research, we developed a cancer-erythrocyte hybrid membrane consisting of a human osteosarcoma cell membrane (HOS-M) and an RBC membrane (RBC-M). The membrane was then used to coat poly(lactic-co-glycolic) acid (PLGA) loaded with Fe<sub>3</sub>O<sub>4</sub>-DHJS (FDP) to fabricate Fe<sub>3</sub>O<sub>4</sub>-DHJS@HRM (FDPM) nanoparticles. Owing to CD47 protein on RBC-M and homologous adhesion domains on HOS-M, the hybrid membrane endowed core nanoparticles with a conspicuous extension of the circulation time in blood and significantly enhanced tumor-targeting capability.<sup>22,28</sup> After FDPM nanoparticles were engulfed by the cancer cells, the synergism of Fe<sub>3</sub>O<sub>4</sub> and DHJS induced lethal ferroptosis in cancer cells. Moreover, after the complete destruction of the intracellular antioxidant system, core FDP nanoparticles under white light irradiation exhibited excellent photodynamic toxicity (PDT) and induced ICD in cancer cells with an increased intensity. This occurrence promoted the emission of sufficient damage-associated molecular patterns (DAMPs) including exposure of calreticulin (CRT) at the cell surface and the release of high-mobility group box 1 (HMGB1) and ATP into the tumor microenvironment (TME).<sup>29</sup> In addition, we found that FDP nanoparticles could promote the recruitment of macrophages and induce macrophage polarization from M2 to M1. The polarized M1 macrophage released a large amount of H<sub>2</sub>O<sub>2</sub> into the TME<sup>10,12,30</sup> and thus promoted the Fenton reaction with Fe ions released from FDP nanoparticles. The polarized M1 macrophage and tumor-associated antigens (TAAs) such as DAMPs and tumor antigens of HRM synergistically achieved TME immunomodulation.<sup>31–37</sup> Using two osteosarcoma animal models, we systematically demon-

strated that FDPM nanoparticles exerted excellent anticancer therapeutic effects via the synergism of ferroptosis and photodynamic immunomodulation.

## RESULTS AND DISCUSSION

**Effects of Fe<sub>3</sub>O<sub>4</sub> Nanoparticles on Oxidative Homeostasis in HOS Cells.** To explore the effects of Fe<sub>3</sub>O<sub>4</sub> nanoparticles on oxidation and the antioxidant systems of cancer cells, we analyzed the RNA-seq and microarray data sets from GEO (GSE15248).<sup>14</sup> The limma package in R was used to analyze the Fe<sub>3</sub>O<sub>4</sub> nanoparticle data set, and the screening criteria were  $|\log_{2}FC| \geq 2$  and FDR < 0.05. The results showed 422 differentially expressed genes (DEGs), including 139 upregulated genes and 283 downregulated genes (Figure 1A). KEGG pathway enrichment analyses for these DEGs were performed using the “org.Hs.eg.db”, “clusterProfiler”, and “enrichplot” packages in R. Upregulated genes related to the oxidation system were found to be mainly enriched in signaling pathways such as “Ferroptosis”, “Transcriptional activation by NRF2 in response to phytochemicals”, and “NRF2-ARE regulation”. By contrast, downregulated genes were enriched in signaling pathways such as “DNA repair pathways”, “DNA replication”, “DNA IR-damage and cellular response via ATR”, and “DNA mismatch repair” (Figure 1B). On the basis of the RNA sequencing data analysis, the reason Fe<sub>3</sub>O<sub>4</sub> nanoparticles could not induce lethal ferroptosis in cancer cells may be that cancer cells could activate intracellular antioxidant activity via Nrf2 overexpression (Figure 1C). Nrf2 is an important transcription factor that regulates the expression of a large number of genes in oxidative stress and antioxidant defense, which is made up of 605 amino acids and contains 7 conserved regions known as Nrf2-ECH homology domains.<sup>15</sup> To further assess the importance of Nrf2 against lethal ferroptosis caused by Fe<sub>3</sub>O<sub>4</sub> nanoparticles, we transfected the adenovirus-encoding Nrf2 shRNA or the control adenovirus into HOS cells. We then treated HOS cells (with shRNA-Nrf2 or shRNA-con) with Fe<sub>3</sub>O<sub>4</sub> nanoparticles at different concentrations in 96-well plates (50 adenovirus nanoparticles per well) for 24 h, and the potential toxicity of Fe<sub>3</sub>O<sub>4</sub> nanoparticles on cancer cells was measured with the Cell Counting Kit-8 (CCK8). The CCK8 assay results revealed that the cell proliferation of HOS cells (with shRNA-con) treated with less than 30 μg of Fe/mL was not affected (Figure S1A); meanwhile, the cytotoxicity gradually increased when the Fe<sub>3</sub>O<sub>4</sub> concentration exceeded 10 μg of Fe/mL for cancer cells transfected with shRNA-Nrf2. Western blot analysis revealed that the expression level of Nrf2 in a concentration-dependent manner reached 0–10 μg Fe/mL and reached the plateau at 10–40 μg Fe/mL (Figure 1D,E). Therefore, a Fe<sub>3</sub>O<sub>4</sub> nanoparticle concentration of 10 μg of Fe/mL was chosen for the subsequent study. The aforementioned results confirmed that cancer cells could avoid lethal ferroptosis by overexpressing the Nrf-2 related antioxidant system after treatment with Fe<sub>3</sub>O<sub>4</sub> nanoparticles. This finding provides new implications for the use of Fe<sub>3</sub>O<sub>4</sub> nanoparticles to induce ferroptosis.

Our previous research demonstrated that DHJS, a new organic near-infrared fluorescent probe, exhibited excellent photodynamic activity to cancer cells, which could significantly increase the level of intracellular ROS; however, the mechanism remains unclear.<sup>16</sup> Considering that Nrf-2 acts as a primary line of defense against the accumulation of ROS to maintain oxidative homeostasis, we hypothesized that DHJS could inhibit the expression of Nrf2 in cancer cells. To investigate the effects

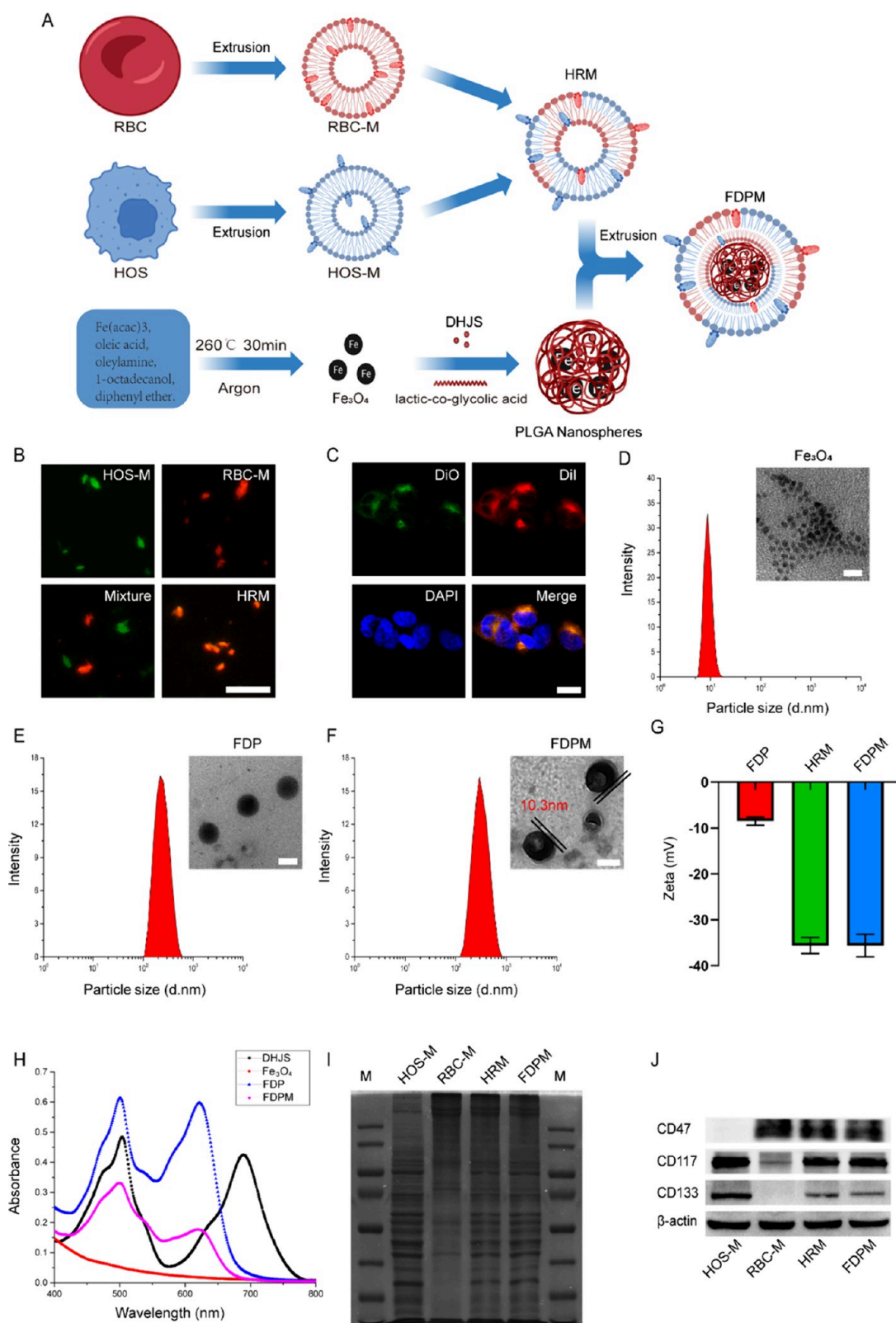


**Figure 2.** Preparation (A) and characterization (B–J) of Fe<sub>3</sub>O<sub>4</sub>-DHJS@HRM nanoparticles. (A) Schematic of membrane fusion (HOS-M and RBC-M), preparation of FDP nanoparticles, and fabrication of FDPM nanoparticles. (B) CLSM images of HOS-M, RBC-M, a mixture of HOS-M and RBC-M, and the hybrid HRM membrane. Scale bar: 5 μm. (C) CLSM images of hybrid HRM cells incubated with HOS cells for 4 h. Scale bar: 20 μm. (D, E, and F) Hydrodynamic size and TEM images of Fe<sub>3</sub>O<sub>4</sub> (scale bar: 20 nm), FDP, and FDPM nanoparticles (scale bar: 200 nm). (G) The ζ potentials of FDP, HRM, and FDPM nanoparticles. (H) UV–vis spectra of DHJS, Fe<sub>3</sub>O<sub>4</sub>, FDP, and FDPM nanoparticles. (I) SDS-PAGE protein analysis of HOS-M, RBC-M, HRM, and FDPM nanoparticles by Coomassie blue staining; M: protein marker. (J) Western blot analysis of HOS-M, RBC-M, HRM, and FDPM nanoparticles for characteristic RBC membrane markers CD47 and HOS cell membrane markers CD117 and CD133.

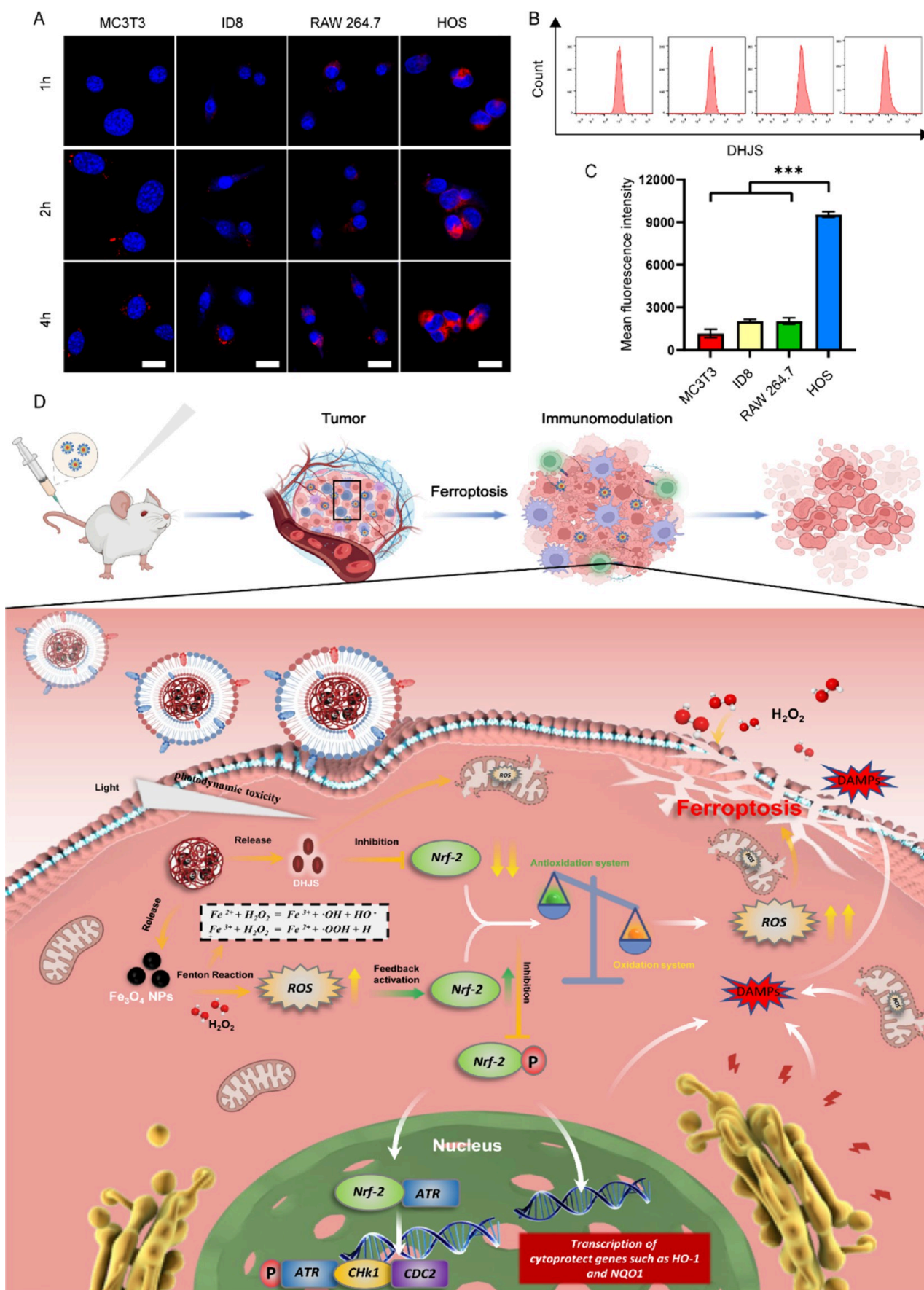


**Figure 3.** Homologous targeting *in vitro* (A–C) and schematic of the mechanism (D) of FDPM nanoparticles. (A) CLSM images and (B and C) Flow cytometry analysis of MC3T3, ID8, RAW 264.7, and HOS cells incubated with FDPM for 1, 2, and 4 h (DHJS:  $\lambda_{ex}$  = 640 nm,  $\lambda_{em}$  = 697 nm). Scale bar:

Figure 3. continued

20  $\mu\text{m}$ . (D) Schematic of the mechanism of FDPM nanoparticles to induce ferroptosis for osteosarcoma treatment. In this study, after Nrf2 translocates into the nucleus, it can activate downstream antioxidant pathways in response to ROS, while also phosphorylating ATM- and RAD3-related (ATR) pathways and subsequently activating the ATR-CHK1-CDC2 signaling pathway in response to DNA damage. In the tumor cells undergoing ICD, the DAMPs derived from damaged mitochondria, nucleus, endoplasmic reticulum and cytoplasm. Data are presented as mean  $\pm$  SEM and were analyzed using unpaired two-sided Student's *t* test (ns: no significance, \**p* < 0.05, \*\**p* < 0.01, \*\*\**p* < 0.001).

of DHJS on the inhibition of the Nrf2 pathway *in vitro*, we first measured the potential toxicity of DHJS on HOS cells. The CCK8 assay results revealed that the viability of HOS cells treated with less than 2  $\mu\text{M}$  DHJS was not affected without white light irradiation (Figure S1B). Therefore, a dose of 2  $\mu\text{M}$  was chosen for further experiments. Subsequently, we evaluated whether DHJS could inhibit the Nrf2 pathway. The Western blot results showed that DHJS markedly inhibited the expression of Nrf2 in a dose-dependent manner (Figure 1F,G). The overall expression level of the Nrf2 pathway and the translation of Nrf2 to the nucleus were inhibited by 2  $\mu\text{M}$  DHJS at almost all time points (Figure 1H,I). The aforementioned results indicated that DHJS could inhibit the expression of Nrf-2 and interrupt the signal transduction of Nrf2.

**RBC-HOS Hybrid Membrane and FDPM Nanoparticle Characterization.** The fabrication process of the cancer-erythrocyte hybrid membrane and FDPM nanoparticles is illustrated in Figure 2A. First, a pair of dyes consisting of 1,1'-dioctadecyl-3,3',3',3'-tetramethylindocarbocyanine perchlorate (DiI) and 3,3'-dioctadecyloxycarbocyanine perchlorate (DiO) was employed to label RBC-M and HOS-M to demonstrate the fusion of the two membranes. We fused the DiO-labeled HOS-M and DiI-labeled RBC-M in a 1:1 protein weight ratio followed by sonication at 37  $^{\circ}\text{C}$  for 10 min. Under confocal laser scanning microscopy (CLSM), significant colocalization of fluorescent signals was observed in the hybrid membrane; in contrast, a direct mixture of ID8-M and RBC-M fabricated using individual dyes showed distinct green and red fluorescent signals (Figure 2B). To further identify the fusion of cell membranes, we incubated double dye-labeled hybrid HRM with HOS cells for 4 h. After adsorption and phagocytosis, the double dye-labeled vesicles exhibited colocalization of fluorescence signals on HOS cells (Figure 2C). The aforementioned results confirmed the successful fusion of HOS-M and RBC-M. Subsequently, we initially identified the successful synthesis of FDP nanoparticles by transmission electron microscopy (TEM). The average diameters of  $\text{Fe}_3\text{O}_4$  nanoparticles and FDP nanoparticles, as visualized by TEM, were 8.4 and 201.2 nm, respectively (Figure 2D,E). Finally, after adding excess HRM to the FDP nanoparticles, we fabricated the FDPM nanoparticles by extrusion and collected the synthetic FDPM nanoparticles by centrifugation. The corresponding diameter of the FDPM nanoparticles was 221.8 nm in size, as observed by TEM (Figure 2F). Compared with that of bare FDP nanoparticles, the size of the nanoparticles coated with the cell membrane uniformly increased by about 220 nm, which was similarly reported in previous studies.<sup>22,38,39</sup>

In assessing their loading efficiencies and capacities, DHJS and  $\text{Fe}_3\text{O}_4$  in the FDPM nanoparticles at different concentrations were used for the synthesis of FDPM nanoparticles. The results showed that DHJS and  $\text{Fe}_3\text{O}_4$  had loading efficiencies of 87.5 and 84.3%, respectively (Figure S2A). Meanwhile, the loading capacities of Fe and DHJS were 210  $\mu\text{g}/10$  mg (PLGA) and 35  $\mu\text{g}/10$  mg (PLGA).

*In vitro*, the long-term stability of FDPM was evaluated by DLS detection, and the size of the synthesized nanoparticle remained almost unchanged for 30 days in both PBS and serum (Figure S2B), suggesting the high stability of the FDPM nanoparticles. In addition, the surface  $\zeta$  potential of the FDP nanoparticles was only  $-8.3$  mV. After HRM coating, the final surface  $\zeta$  potential of the FDPM nanoparticles was  $-35.8$  mV (Figure 2G). Furthermore, UV-vis spectra showed that FDP and FDPM had absorption peaks similar to those of DHJS alone (Figure 2H). SDS-PAGE protein analysis by Coomassie blue staining indicated that numerous membrane protein bands of hybrid HRM were inherited from HOS-M and RBC-M (Figure 2I). CD47, a self-maker of RBC-M that can prevent macrophage uptake,<sup>40,41</sup> and CD133 and CD117, specific markers of HOS-M,<sup>42,43</sup> were detected by Western blot analysis (Figure 2J). In conclusion, the aforementioned results verified the perfect fusion of HOS-M and RBC-M, with the hybrid HRM successfully coated onto the surface of the FDP nanoparticles.

**Cytotoxicity and Homologous Targeting *In Vitro* and *In Vivo*.** The evaluation of the cytotoxicity of the nanoparticles is critical for their biological applications. We cocultured FDPM (10  $\mu\text{g}$  of Fe/mL) nanoparticles at different concentrations of DHJS (0–8  $\mu\text{M}$ ) with HOS cells in 96-well plates for 24 h and detected the cell proliferation by using CCK8.

We found that the cytotoxicity of the particles without white light radiation gradually increased when the DHJS concentration exceeded 1  $\mu\text{M}$ , and the cell viability of HOS decreased to 66.4% at a DHJS concentration of 2  $\mu\text{M}$  (Figure S3A). However, the cytotoxicity of laser-irradiated nanoparticles significantly increased when the DHJS concentration was 0.5  $\mu\text{M}$ , and the cell viability of HOS decreased to 7.5% at 2  $\mu\text{M}$  DHJS (Figure S3A). Therefore, FDPM nanoparticles with a DHJS concentration of 2  $\mu\text{M}$  were chosen for a subsequent study. To further assess the cytotoxicity of FDPM nanoparticles (Fe concentration of 10  $\mu\text{g}/\text{mL}$  and DHJS concentration of 2  $\mu\text{M}$ ) to different types of cells, including the ovarian cancer cell line (ID8), osteoblast cell line (MC3T3), and immune cell line (RAW 264.7), we incubated FDPM nanoparticles with these cell lines for 24 h with or without light irradiation. No significant cytotoxicity was found after treatment for 24 h without light irradiation for the other three types of cells; meanwhile, when these cells received light radiation, the cell viabilities of ID8, MC3T3, and RAW 264.7 were approximately 57.6, 63.1, and 43.8%, respectively (Figure S3B).

To examine the homologous targeting ability of synthesized FDPM nanoparticles, we incubated FDPM nanoparticles with HOS, ID8, MC3T3, and RAW 264.7 cells for 1, 2, and 4 h, respectively. As illustrated in Figure 3A, stronger red fluorescence signal than that of the other three types of cells was detected in HOS cells at all time points by using CLSM. Quantitative flow cytometry analysis (FCM) further demonstrated that the mean fluorescence intensity (MFI) of HOS cells was approximately 8.3-fold higher than that of MC3T3 cell and about 4.7- and 4.5-fold higher than those of ID8 and RAW 264.7 cells at 4 h (Figure 3B,C). These results mean that HOS cells

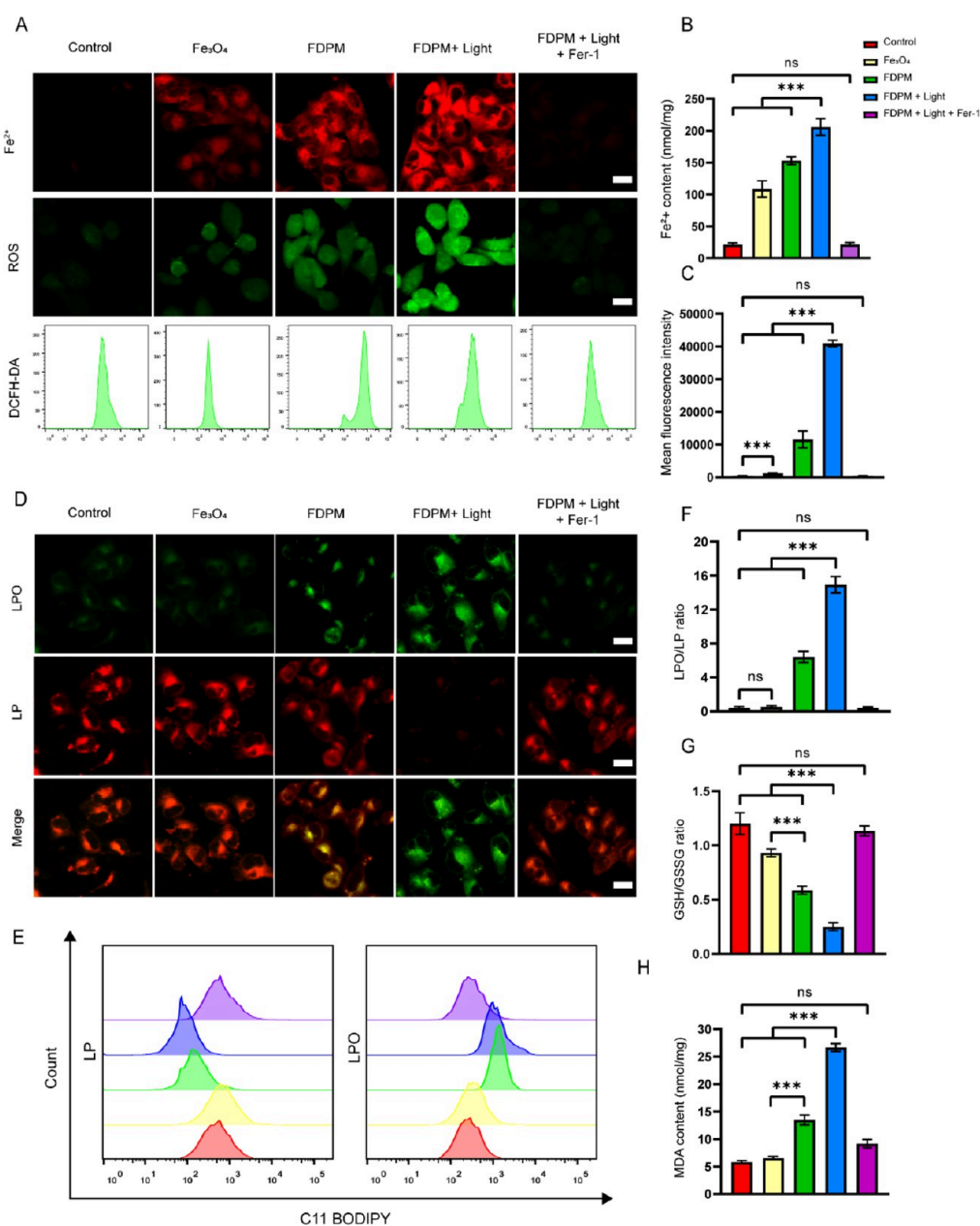


**Figure 4.** DHJS can synergize with Fe<sub>3</sub>O<sub>4</sub> nanoparticles to trigger lethal ferroptosis in HOS cells. (A) Detection of Fe<sup>2+</sup> and ROS in HOS cells after different treatments using fluorescence probes by CLSM or FCM (FerroOrange:  $\lambda_{\text{ex}} = 542$  nm,  $\lambda_{\text{em}} = 572$  nm; DCFH-DA:  $\lambda_{\text{ex}} = 488$  nm,  $\lambda_{\text{em}} = 525$  nm). Scale bar: 20  $\mu\text{m}$ . (B) Quantitative detection of intracellular Fe<sup>2+</sup> in HOS cells after different treatments. (C) Quantitative analysis of the ROS fluorescence intensity in HOS cells. (D) CLSM images of immunofluorescence staining of LPO and LP in HOS cells after different treatments. Green fluorescence represents LPO ( $\lambda_{\text{ex}} = 488$  nm,  $\lambda_{\text{em}} = 510$  nm), and red fluorescence denotes LP ( $\lambda_{\text{ex}} = 581$  nm,  $\lambda_{\text{em}} = 591$  nm). Scale bar: 20  $\mu\text{m}$ . (E, F) Quantitative analysis of LPO/LP fluorescence intensity in HOS cells by flow cytometry. (G, H) Quantitative detection of intracellular GSH (G) and MDA (H) contents in HOS cells after different treatments. Data are presented as mean  $\pm$  SEM and were analyzed using unpaired two-sided Student's *t* test (ns: no significance, \**p* < 0.05, \*\**p* < 0.01, \*\*\**p* < 0.001).

exhibit a higher uptake rate of FDPM nanoparticles than the other cell lines at the same time points, which is likely caused by the excellent self-recognition capability of the hybrid membrane.

To further investigate the targeting specificity of FDPM for HOS cells, we intravenously injected HOS-bearing nude mice with FDPM nanoparticles. In addition, FDP@RBC-M and FDP@HOS-M (DHJS concentration of 5 mg/kg) were used as controls. After 24 h, the tumors and major organs in the FDPM, FDP@RBC-M, and FDP@HOS-M groups were collected and examined. The results obtained using the IVIS system indicated that these different kinds of nanoparticles were mainly

concentrated in the liver, kidney, and tumors (Figure S3C,D). Compared with those of the FDP@RBC-M and FDP@HOS-M groups, the FDPM group showed a stronger fluorescent signal in the tumors at 24 h postinjection. This difference could be attributed to the improved circulation life and enhanced homologous targeting ability derived from the hybrid membrane. The results obtained using the IVIS system indicated that the accumulation of FDP nanoparticles in the FDPM group was 1.7- and 3.6-fold those of the FDP@RBC-M and FDP@HOS-M groups (Figure S3C,D), demonstrating that FDPM could specifically accumulate in the tumors. These experimental

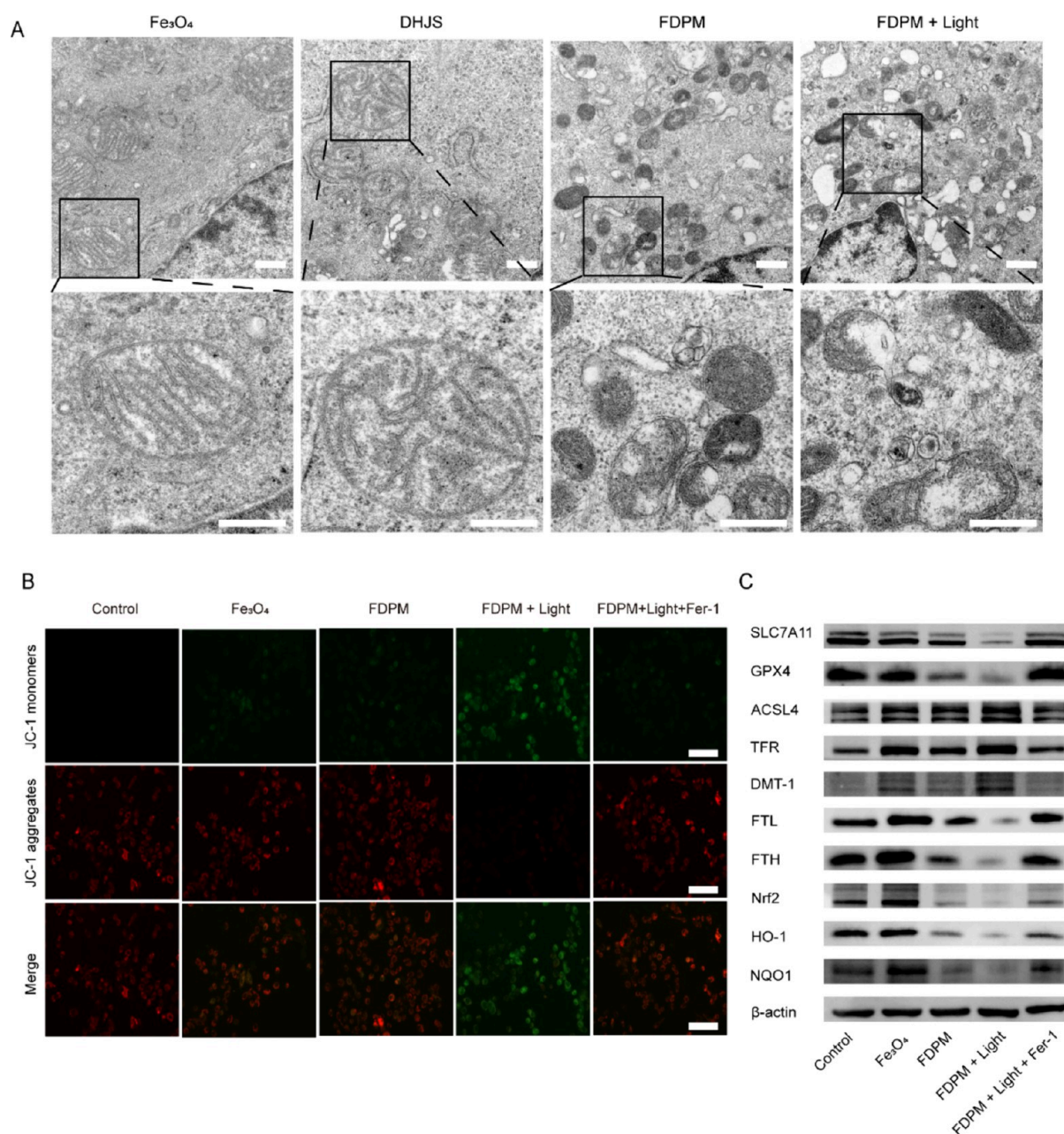


**Figure 5.** Molecular mechanism by which FDPM induces ferroptosis in cancer cells. (A) Morphological assessment of mitochondria by bio-TME after treatment of HOS cells with various nanoparticles. Scale bar: 500 nm. (B) Mitochondrial transmembrane potential of HOS cells after different treatments tested using JC-1 fluorescent probes. Green fluorescence represents JC-1 monomers ( $\lambda_{\text{ex}} = 514 \text{ nm}$ ,  $\lambda_{\text{em}} = 529 \text{ nm}$ ), and red fluorescence denotes JC-1 aggregates ( $\lambda_{\text{ex}} = 585 \text{ nm}$ ,  $\lambda_{\text{em}} = 590 \text{ nm}$ ). Scale bar: 100 nm. (C) WB analysis showing the protein expression levels of Fe metabolism, Nrf2-related, and ferroptosis pathways in HOS cells after different treatments.  $\beta$ -Actin is used as the internal reference. Data are presented as mean  $\pm$  SEM and were analyzed using unpaired two-sided Student's *t* test (ns: no significance, \**p* < 0.05, \*\**p* < 0.01, \*\*\**p* < 0.001).

results *in vivo* and *in vitro* showed that compared with the RBC-M and HOS-M coating strategies, the fused membrane coating strategy endowed the PLGA nanomicrosphere with superior capability for homologous targeting.

As demonstrated in Figure 3D, following the targeted delivery of core nanoparticles into tumor cells through hybrid HRM, PLGA gradually released DHJS and iron oxide within the cytoplasm. Iron oxide, on one hand, facilitates intracellular ROS production, whereas tumor cells in response activate the Nrf2-related pathway to counteract the accumulated ROS. Conversely, DHJS exerts a notable inhibitory effect on Nrf2 overexpression and disrupts the cellular antioxidant system,

leading to excessive intracellular ROS and LPO levels. Upon exposure to light radiation, DHJS demonstrates remarkable photodynamic toxicity, rapidly elevating intracellular ROS levels and inducing more comprehensive ICD. Consequently, this process liberates DAMPs into the surrounding tissues, thereby activating the immune system.

**Efficiency and Mechanism of Ferroptosis Therapy on Cancer Cells.** Prompted by the homologous targeting ability of synthesized FDPM nanoparticles *in vitro* and *in vivo*, we carefully examined the anticancer performance of FDPM nanoparticles *in vitro*. Aberrant iron metabolism, ROS generation, and abnormal rate of LPO/LP are the hallmarks of ferroptosis.<sup>6,44</sup> First, after

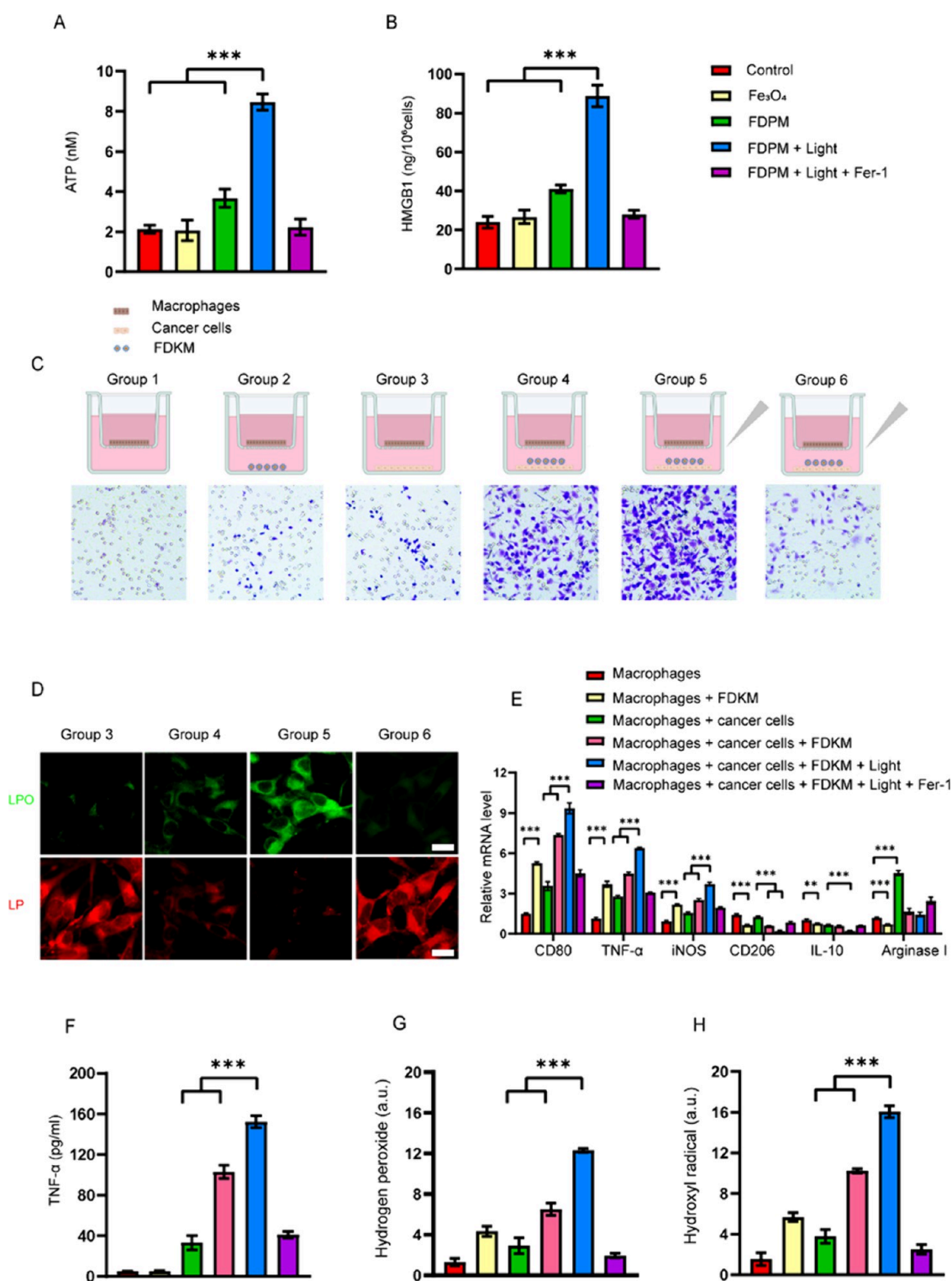


**Figure 6.** The combination of FDKM and DAMPs promotes the migration and M1 polarization of macrophages *in vitro*. (A, B) Quantitative detection of ATP (A) and HMGB1 (B) in HOS cells after different treatments. (C) Migration assays of BMM cells in Transwell inserts induced by FDKM nanoparticles or DAMPs from K7M2 cells, detected by crystal violet staining. Group 1: macrophages alone; group 2: coculture of macrophages and FDKM; group 3: coculture of macrophages and cancer cells; group 4: coculture of macrophages, cancer cells, and FDKM; group 5: coculture of macrophages, cancer cells, and FDKM irradiated with white light; and group 6: under white light radiation, coculture of macrophages, cancer cells, and Fer-1. (D) Coculture of cancer cells, macrophages, and FDKM nanoparticles irradiated with light, leading to significantly increased LPO/LP level in cancer cells. Scale bar: 20 μm. (E) Relative mRNA levels of M1-related genes (CD80, TNF-α, and iNOS) and M2-related genes (CD206, IL-10, and arginase I) of BMM cells in different coculture systems detected by RT-PCR. (F) Protein levels of M1-related immunoinflammatory cytokines (TNF-α) with different treatments detected using ELISA kits. (G, H) Quantification of hydrogen peroxide (G) and hydroxyl radicals (H) in coculture systems detected using ELISA kits. Data are presented as mean ± SEM and were analyzed using unpaired two-sided Student's *t* test (ns: no significance, \**p* < 0.05, \*\**p* < 0.01, \*\*\**p* < 0.001).

the treatment of these nanoparticles at the same Fe concentration (10  $\mu\text{g}/\text{mL}$ ), the  $\text{Fe}^{2+}$  content and ROS level were evaluated in HOS cells via a fluorescent probe detected by CLSM or FCM. Compared with the  $\text{Fe}_3\text{O}_4$  group alone, a stronger  $\text{Fe}^{2+}$  and ROS fluorescent signal could be observed in the FDPM group. After laser irradiation, the cells treated with FDPM nanoparticles showed an enhanced fluorescence signal (Figure 4A). The unstable  $\text{Fe}^{2+}$  content in the FDPM + Light group was approximately 1.3- and 1.9-fold higher than those in the FDPM and  $\text{Fe}_3\text{O}_4$  groups as determined by using quantitative assay kits (Figure 4B). Quantitative FCM analysis further demonstrated that the MFI of ROS in the FDPM + Light group was approximately 1.2- and 10.8-fold higher than those in the FDPM group and PBS control groups (Figure 4A–C). Subsequently, the C11 BODIPY fluorescent probe was used to detect cellular LPO. High cellular green LPO fluorescence was observed only when FDPM was exposed to laser irradiation, as determined from the CLSM images (Figure 4D). Quantitative FCM analysis further demonstrated that the LPO/LP value in the FDPM + Light group was about 2.3-fold higher than that in the FDPM group (Figure 4E,F). GSH is a major cellular redox buffer and an important indicator of redox status in cells. We detected the GSH/GSSG ratio by using the assay kit, the trend variation of which was similar to that of the protein expression of GSH-related genes (Figure 4G). As a product generated from LPO, MDA was also used as one of the classic ferroptosis markers. In this study, the fluctuation trend of the MDA content was similar to that of LPO (Figure 4H). Meanwhile, ferrostatin-1 (Fer-1) is an efficient ferroptosis specific inhibitor, which functions by eliminating the initiating alkoxyl radicals and other rearrangement products generated by ferrous iron from lipid hydroperoxides.<sup>45</sup> To confirm the existence of ferroptosis, we used Fer-1 (10  $\mu\text{M}/\text{mL}$ ) to conduct a rescue experiment *in vitro* in this study. Fer-1 reduced the content of unstable iron particles and scavenged the accumulation of oxidized free radicals and the proportion of LPO in the cell membranes (Figure 4A–H), avoiding ferroptosis in HOS cells.

The abnormal alteration in the mitochondrial membrane potential is not only an important marker of mitochondrial damage but also an early warning of ferroptosis.<sup>46</sup> For more visual observation of cellular ferroptosis, we examined the morphology of the HOS cells by TEM. The cells treated with FDPM or  $\text{Fe}_3\text{O}_4$  nanoparticles exhibited only evident swelling of mitochondria, which was consistent with previous reports. Nonetheless, TEM demonstrated a large number of shrunken mitochondria, an increase in the density of the mitochondrial membrane, and a reduction (or the disappearance) of mitochondrial cristae in the FDPM group (Figure 5A), which were typical morphological features of ferroptosis. A JC-1 fluorescent probe was used to detect alterations in the mitochondrial membrane potential. The mitochondrial membrane potential markedly decreased with intensified green fluorescence in the FDPM + Light group (Figure 5B), indicating the increased proportion of HOS cells with depolarized mitochondria. Combining the aforementioned results, we systemically confirmed that FDPM nanoparticles exposed to laser irradiation could trigger lethal ferroptosis in cancer cells.

To explore the mechanism by which FDPM induced ferroptosis in cancer cells, we determined the protein expression of the genes related to the Fe metabolism, Nrf2, and ferroptosis pathways by Western blot analysis. We used the protein expression levels of SLC7A11, GPX4, and ACSL4 as markers of ferroptosis; the protein expression levels of TFR, DMT-1, FTH,

and FTL as markers of Fe metabolism; and the protein expression levels of Nrf-2, HO-1, and HOQ1 as markers of Nrf2-related pathway genes (Figure 5C). Using Western blot analysis, we found that  $\text{Fe}_3\text{O}_4$  nanoparticles could increase the protein expression of the intracellular genes related to iron endocytosis (TFR), transport (DMT-1), and storage (FTH and FTL) (Figure 5C and Figure S4). An increase in intracellular Fe can arise from TFR-mediated Fe import or ferritin degradation. Therefore, the increase in  $\text{Fe}^{2+}$  in the HOS cell treated with  $\text{Fe}_3\text{O}_4$  nanoparticles alone could only be attributed to the increased cellular Fe uptake. Nrf2 is known to be the first defense against oxidation stress; Nrf2 and its downstream genes, such as HO-1 and NQO-1, constitute the mainstream of the cellular antioxidant system. In addition, Nrf2 plays an important role in alleviating lipid peroxidation and ferroptosis.<sup>47,48</sup> In the FDPM group, DHJS could significantly inhibit the overall protein expression of the Nrf2-related genes. In this study, the protein expression levels of TFR and DMT-1 in the cells treated with FDPM were lower than those in cells treated with  $\text{Fe}_3\text{O}_4$  alone (Figure 5C and Figure S4). However, the  $\text{Fe}^{2+}$  content in the FDPM group was higher than that in the  $\text{Fe}_3\text{O}_4$  group (Figure 4B). The unexpected results suggested that the higher  $\text{Fe}^{2+}$  content in HOS cells in the FDPM group could be attributed partly to the TFR-mediated Fe import and partly to ferritin degradation, such as FTH and FTL (Figure 5C and Figure S4). The reason could be the downregulation of Nrf2 caused by DHJS. The protein expression level of the GSH-related genes (SLC7A11 and GPX4) and the lipid metabolism-related gene ACSL4 remarkably decreased in the FDPM + Light group relative to that in the group treated with FDPM nanoparticles alone (Figure 5C and Figure S4). Further, Fer-1 could significantly rescue the expression of these genes (Figure 5C and Figure S4). The band density ratios of the aforementioned genes to  $\beta$ -actin in the Western blots were quantified by densitometry, and the difference in the protein band density ratio was statistically significant. On the basis of the aforementioned results, we concluded that FDPM nanoparticles triggered lethal ferroptosis in HOS cells via the regulation and control of the Fe metabolism-related and Nrf2-related pathways.

#### Synergism of Immunomodulation and Ferroptosis.

One of the main characteristics of ICD is the emission of DAMPs, such as the surface exposure of CRT and the release of HMGB1 and ATP. To determine the immunogenicity of ferroptosis induced by FDPM nanoparticles, we incubated the nanoparticles with HOS cells in six-well plates for 24 h.

Compared with those in the PBS and FDPM groups, the HOS cells induced by FDPM released large amounts of HMGB1 and ATP (Figure 6A,B), which were associated with plasma membrane rupture.<sup>49</sup> Considering that the HOS cell was a human-derived osteosarcoma cell line, we selected the murine-derived osteosarcoma cell line K7M2 to conduct immunomodulation-related experiments. Meanwhile, similar to the synthesis process illustrated in Figure 2A, we used the hybrid membrane consisting of the K7M2 cell membrane and RBC membrane to coat the PLGA nanomicrosphere and fabricated  $\text{Fe}_3\text{O}_4$ -DHJS@KRM (FDKM) nanoparticles (Fe concentration 10  $\mu\text{g}/\text{mL}$  and DHJS concentration at 2  $\mu\text{M}$ ). Using Western blot analysis, we again determined that FDKM nanoparticles triggered lethal ferroptosis in K7M2 cells via the regulation and control of the Fe metabolism-related and Nrf2-related pathway (Figure 5S,A,B).

To determine whether FDKM nanoparticles attracted macrophages, we constructed a dual-chamber coculture system

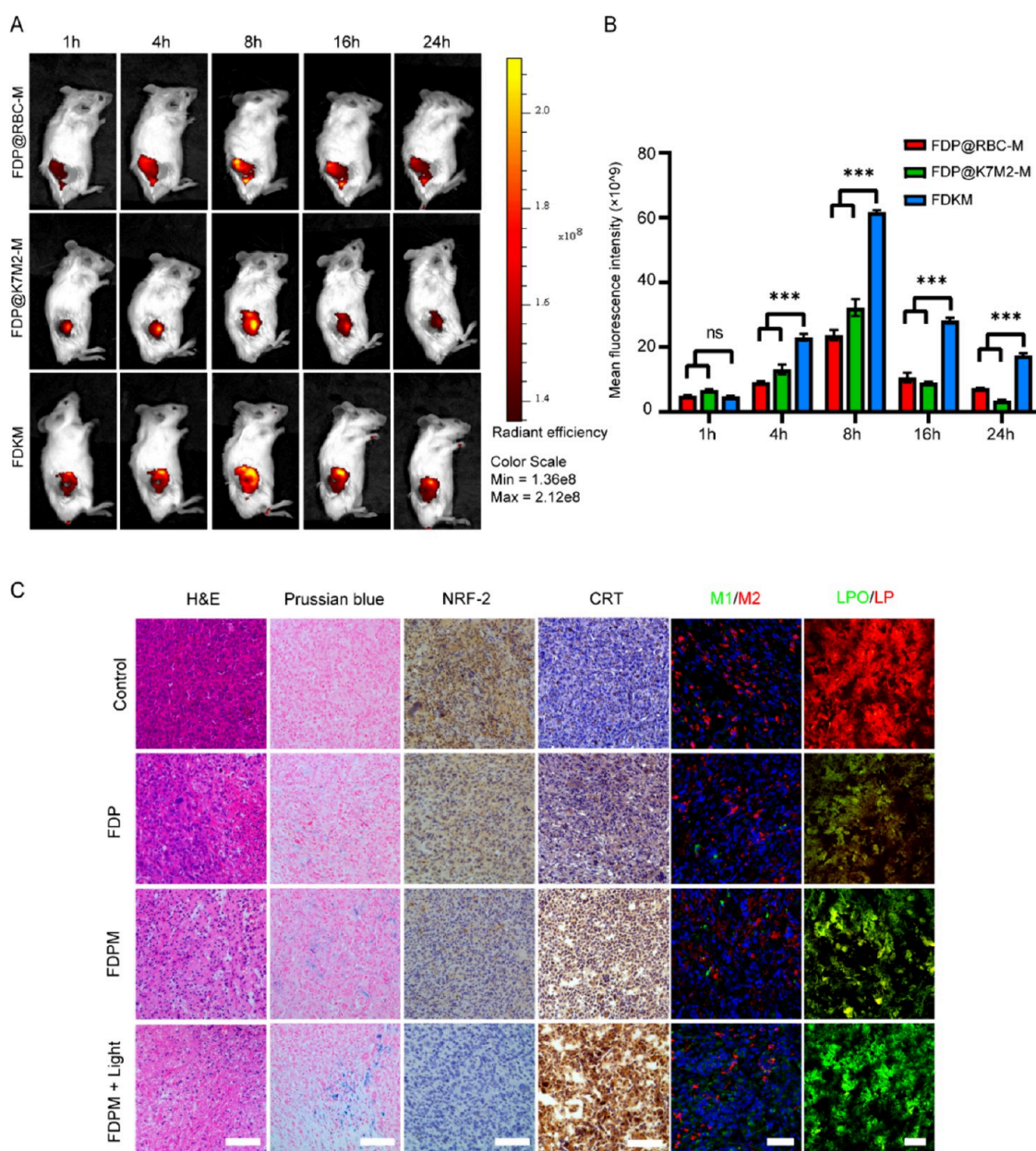


**Figure 7.** Homologous targeting ability (A, B), macrophage M1 polarization ability, and antitumor performance (C) of FDKM *in vivo*. (A, B) *In vivo* fluorescence images showing tumor retention of FDP@RBC-M, FDP@K7M2-M, and FDKM over a span of 24 h after intravenous administration into the tail vein in K7M2 tumor-bearing mice (DHJS:  $\lambda_{ex} = 640$  nm,  $\lambda_{em} = 710$  nm,  $n = 3$ ). (C) Histological evaluation of tumor tissues in K7M2 tumor-bearing mice after different treatments ( $n = 5$ ). Prussian blue staining was conducted to determine iron content in tumors. Staining of IHC images with antibodies against NRF2, CRT, and the BODIPY-C11 probe (green fluorescence represents LPO, and red fluorescence denotes LP). Immunofluorescence staining of CD80 and CD206 to assess the ratio of M1- to M2-associated macrophages (green fluorescence represents M2 macrophages, and red fluorescence denotes M1 macrophages). Scale bar: 100  $\mu$ m. Data are presented as mean  $\pm$  SEM and were analyzed using unpaired two-sided Student's *t* test (ns: no significance, \* $p < 0.05$ , \*\* $p < 0.01$ , \*\*\* $p < 0.001$ ).

with 8- $\mu$ m-sized microporous membranes. After coculture for 24 h, we first evaluated the migration of macrophages toward FDKM nanoparticles, malignant cells, and both by crystal violet staining (Figure 6C). The FDKM + Light group showed a higher capability for macrophage migration than the FDKM group alone, and Fer-1 could inhibit macrophage migration induced by the FDKM nanoparticles (Figure 6C and Figure S5C). In addition, a larger amount of LPO was produced in K7M2 cells in the FDKM + Light group than in other groups, and Fer-1 significantly scavenges excess intracellular LPO (Figure 6D). The reason could be that PDT induced ICD in K7M2 cells and then released HMGB1 and ATP, promoting

macrophage migration. To further determine if FDKM itself induced the M1 polarization of macrophages, we isolated macrophages from the coculture system and detected the differences in the expression of M1 in contrast to the M2-type mRNAs via RT-PCR. The results indicated that compared with macrophages without any treatment, FDKM-exposed macrophages upregulated the expression of M1-related genes, such as TNF- $\alpha$  and CD80, as well as downregulated the expression of M2-related genes, such as IL-10 and CD206 (Figure 6E). The macrophages in the FDKM + Light group exhibited more significant M1 polarization than that in the FDKM group (Figure 6F). Taken together, the FDKM nanoparticles and

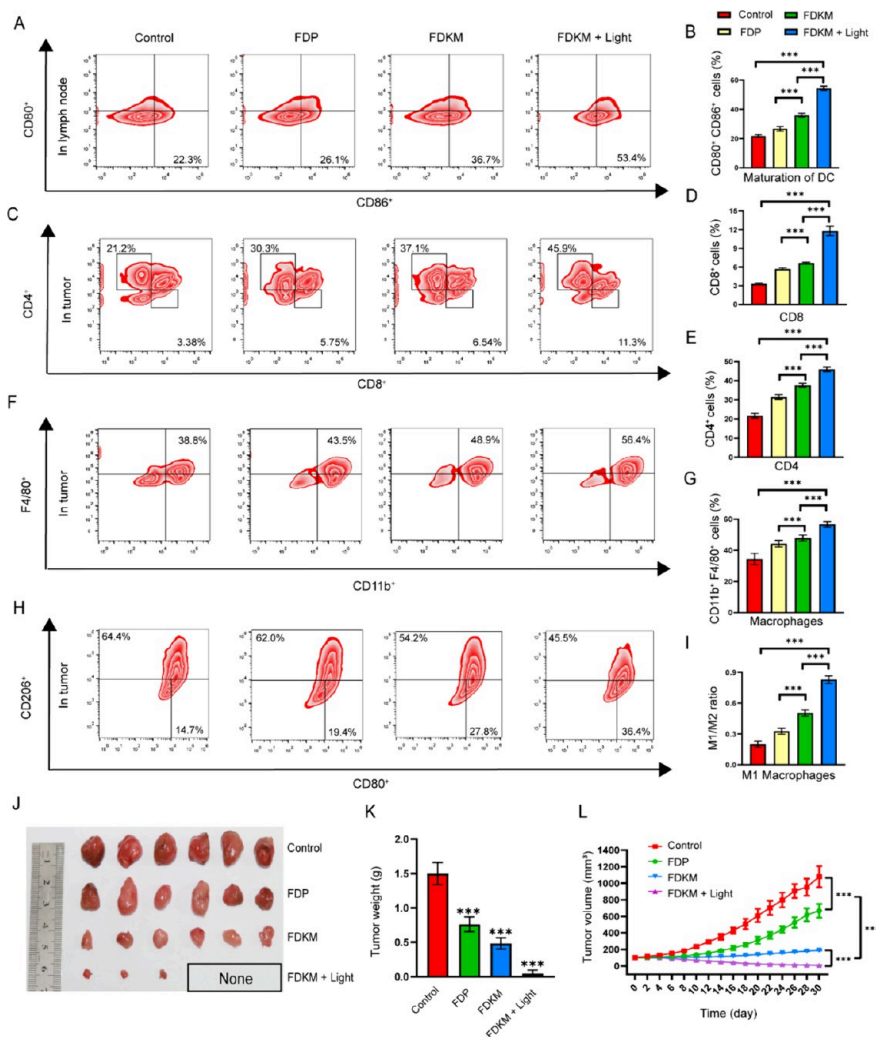


**Figure 8.** Immune activation ability of FDKM *in vivo*. (A, B) Flow cytometric analysis images (A) and statistical data (B) of *in vivo* DC maturation in tumor-draining lymph nodes of K7M2 tumor-bearing mice in each group collected after different treatments for assessment by staining with CD11c, CD80, and CD86 ( $n = 5$ ). (C, D, and E) Flow cytometric analysis images (C) and statistical data (D, E) of the proportions of CD4<sup>+</sup> (CD45<sup>+</sup>CD3<sup>+</sup>CD4<sup>+</sup>) and CD8<sup>+</sup> (CD45<sup>+</sup>CD3<sup>+</sup>CD8<sup>+</sup>) T cells in tumors in each group after different treatments ( $n = 5$ ). (F, G) Flow cytometric analysis images (F) and statistical data (G) for the population of macrophages (CD45<sup>+</sup>CD11b<sup>+</sup>F4/80<sup>+</sup>) in the tumor mass of K7M2 tumor-bearing mice after different treatments ( $n = 5$ ). (H, I) Flow cytometric analysis images (H) and statistical data (I) of the proportion of M1 macrophages (CD45<sup>+</sup>CD11b<sup>+</sup>F4/80<sup>+</sup>CD206<sup>-</sup>) in the tumor mass of K7M2 tumor-bearing mice after different treatments ( $n = 5$ ). (J, K, and L) Tumor size and tumor growth curves for K7M2 tumor-bearing mice recorded every 3 days after different treatments ( $n = 6$ ). Data are presented as mean  $\pm$  SEM and were analyzed using unpaired two-sided Student's *t* test (ns: no significance, \* $p < 0.05$ , \*\* $p < 0.01$ , \*\*\* $p < 0.001$ ).

DAMPs induced macrophage polarization from M2 to M1, and their combination led to an additive effect on the macrophages. Polarized M1 macrophages have been reported to release a large amount of H<sub>2</sub>O<sub>2</sub> to promote the Fenton reaction with Fe<sup>2+</sup> and then generate hydroxyl radical ( $\cdot$ OH), triggering lethal ferroptosis to tumor cells.<sup>30</sup> To confirm if the Fenton reaction occurred in our coculture system, we detected the level of ROS and LPO in cocultures. The cocultures in the FDKM + Light group demonstrated a 4.8-fold increase in the level of H<sub>2</sub>O<sub>2</sub> and a 4.2-fold increase in the level of  $\cdot$ OH generation relative to those in K7M2 cells and macrophages alone (Figure 6G,H).

The superior ferroptosis-inducing capacity and immunomodulation performance *in vitro* prompted us to conduct animal studies *in vivo*. For this purpose, we first needed to verify the homologous targeting ability of synthesized FDKM nanoparticles and identify the best treatment time point with white light radiation *in vivo*. These K7M2 tumor-bearing mice were intravenously injected with FDP@RBC-M, FDP@K7M2-M, or

FDKM (DHJS concentration of 5 mg/kg) and detected at the 1, 4, 8, 16, and 24 h time points by an IVIS imaging system (Figure 7A). The fluorescence signal was increasingly enhanced within 8 h and gradually decreased in all groups (Figure 7A,B). Meanwhile, the strongest fluorescence signal was observed in the FDKM group at the 8 h time point, which is nearly 2.6- and 1.9-fold relative to those in the FDP@RBC-M and FDP@K7M2-M groups, respectively (Figure 7B). Therefore, 8 h was chosen as the time point for white light radiation after intravenous injection for the antitumor experiment *in vivo*. In addition, the hybrid membrane composed of RBC-M could prolong the circulation lifetime of core nanoparticles.<sup>22,38</sup> We further assessed the blood retention of the FDP@RBC-M, FDP@K7M2-M, and FDKM nanoparticles over a span of 24 h (Figure S6A). Compared with the FDP@K7M2-M group, which had blood retention of only 10.1% ID/g, the FDP@RBC-M and FDKM groups maintained blood retention levels of 26.2 and 18.0% ID/g, respectively, after metabolism for 24 h. The

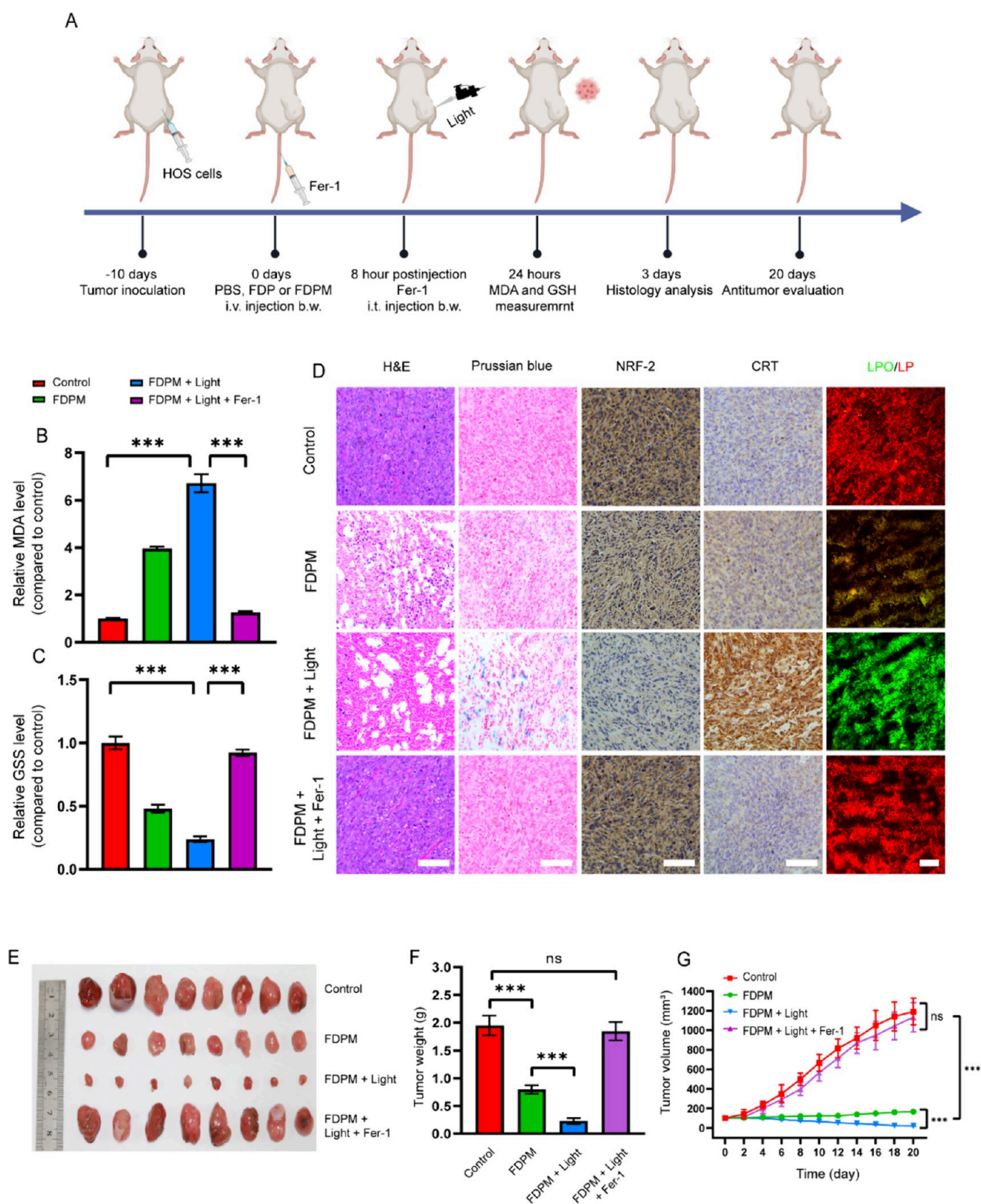


**Figure 9.** Antitumor performance of FDPM *in vivo*. (A) Schematic of the strategy of HOS tumor-bearing nude mice for different treatments. (B, C) Quantitative detection of GSH (B) and MDA (C) contents in the tumor mass in each group with different treatments ( $n = 5$ ). (D) Histological evaluation of tumor tissues of HOS tumor-bearing nude mice after different treatments ( $n = 5$ ). Prussian blue staining was conducted to indicate the iron content in the tumor. Immunohistochemistry images were stained with antibodies against NRF2, CRT, and the BODIPY-C11 probe (green fluorescence denotes LPO, and red fluorescence represents LP). Scale bar: 100  $\mu\text{m}$ . (E, F, and G) Tumor size and tumor growth curves for HOS tumor-bearing nude mice recorded every 2 days after different treatments ( $n = 8$ ). Data presented as mean  $\pm$  SEM and analyzed using unpaired two-sided Student's *t* test (ns: no significance, \* $p < 0.05$ , \*\* $p < 0.01$ , \*\*\* $p < 0.001$ ).

circulation half-life of the FDKM nanoparticles was calculated to be 8.9 h, which was much longer than that of the FDP@K7M2-M nanoparticles (4.3 h) but slightly shorter than that of the FDP@RBC-M nanoparticles (10.9 h). Therefore, FDKM exhibited excellent blood retention properties derived from RBC-M.

To further assess the antitumor effect of FDKM nanoparticles and investigate whether nanoparticles could achieve TME immunomodulation, we constructed a K7M2 tumor-bearing mouse model (Figure S6B). All tumor-bearing mice with a tumor size of  $\sim 100 \text{ mm}^3$  were randomly divided into four groups ( $n = 5$ ) and then treated with PBS, FDP, FDKM, and FDKM + Light, respectively. PBS, FDP, and FDKM nanoparticles were intravenously injected. After 8 h, the FDKM + Light group ( $100 \text{ W/cm}^2$ ) was exposed to white light irradiation for 15 min. After 3 days, the tumors were collected for histological analysis, including hematoxylin–eosin (H&E), immunohistochemistry (IHC), immunofluorescence (IF), Prussian blue staining, and LPO staining, to confirm the ferroptosis induction of the FDKM nanoparticles in the tumor tissue. Through H&E staining, the most severe tissue damage was observed in the FDKM + Light group (Figure 7C). Meanwhile, more significant cellular iron accumulation in the tumor slices was observed in the FDKM + Light group (Figure 7C). A significant inhibitory effect of Nrf2 was observed in the FDKM + Light group, relative to that in the PBS group, in the following order: FDP < FDKM < FDKM + Light (Figure 7C). In addition, the upregulation of CRT on the surface of cancer cells was observed only when the FDKM nanoparticles were exposed to laser irradiation (Figure 7C). We thus determined that dying cancer cells induced by FDKM with laser irradiation were immunogenic. IF analysis showed that, relative to that in other groups, the value of M1/M2 macrophages within tumor sections in the FDKM + Light group markedly increased (Figure 7C), representing increased quantities of proinflammatory M1 macrophages in cancers. Relative to that in the PBS group, the generation of LPO was markedly increased in the tumor upon simultaneous exposure to FDKM nanoparticles and laser irradiation (Figure 7C).

To explore the changes of immune microenvironment in tumor tissue after nanodrug intervention, tumor-bearing mice with a tumor size of  $\sim 100 \text{ mm}^3$  were randomly divided into four groups ( $n = 5$ ). After treatment for 8 days, the tumor and draining lymph nodes (LNs) were collected and further processed into single-cell suspensions, and the immune cell subsets were detected by FCM analysis.<sup>24</sup> In draining LNs (Figure 8A), in comparison with the PBS group ( $21.6 \pm 1.0\%$ ) and FDP group ( $26.7 \pm 1.6\%$ ), treatment with FDKM nanoparticles ( $36.0 \pm 1.3\%$ ) markedly promoted the maturation of DCs (including  $\text{CD80}^+$ ,  $\text{CD86}^+$ , and  $\text{CD80}^+$  plus  $\text{CD86}^+$  cell population), and the increase was more significant in the FDKM + Light group ( $54.4 \pm 1.4\%$ ) (Figure 8B). The CTL levels in tumors in all groups were also analyzed. As shown in Figure 8C, the FDKM + Light group demonstrated the highest population of CTLs in the tumor ( $11.8 \pm 0.7\%$ ) compared with the other groups of the control ( $3.3 \pm 0.1\%$ ), FDP ( $5.7 \pm 0.2\%$ ), and FDKM ( $6.6 \pm 0.1\%$ ) (Figure 8C,D).  $\text{CD4}^+$  T cells are critical for the induction and maintenance of the  $\text{CD8}^+$  T cell response in tumors. In addition,  $\text{CD4}^+$  T cells are essential for the generation and robust expansion of functional memory of the  $\text{CD8}^+$  T cell population.<sup>50</sup> Notably,  $\text{CD4}^+$  T cell infiltration in tumors was also highest in the FDKM + Light group ( $45.9 \pm 1.2\%$ ) among all groups, suggesting that FDKM nanoparticles exhibited

enhanced antitumor vaccine effects (Figure 8C,E). Compared with the PBS group ( $34.3 \pm 3.5\%$ ) and FDP group ( $44.2 \pm 2.1\%$ ), the FDKM ( $47.8 \pm 1.9\%$ ) and FDKM + Light ( $56.6 \pm 1.9\%$ ) groups demonstrated higher quantities of (tumor association macrophage) TAMs (Figure 8F,G). After laser irradiation, the FDKM nanoparticles induced an increase in the ratio of M1/M2 macrophages ( $\text{CD80}^+\text{CD206}^- \text{ F4/80}^+/\text{CD206}^+ \text{ F4/80}^+$ ) in TME from 0.20 ( $0.20 \pm 0.03$ ) to 0.83 ( $0.83 \pm 0.04$ ) (Figure 8H,I). The stronger activation of the immune system in the FDKM group compared with the FDP group could be attributed to the homologous targeting and antitumor immunotherapy effect of the hybrid membrane in FDKM nanoparticles. Given the combined results, we found that treatment with the FDKM nanoparticles induced immunological responses, including DC maturation in draining LNs, macrophage M1 polarization in tumors, and T cell activation in tumors.

Finally, we assessed the antitumor effect of FDKM nanoparticles using the K7M2 tumor-bearing model. All tumor-bearing mice with a tumor size of  $\sim 100 \text{ mm}^3$  were randomly divided into four groups ( $n = 6$ ). The tumor size and the body weight were recorded within 30 days, and the tumor weight was measured at 30 days. The tumor size was markedly inhibited in the FDKM + Light group (Figure 8J–L), whereas the variations in the average body weight were negligible under different treatments (Figure S7). These results demonstrated that FDKM nanoparticles exposed to laser irradiation showed a superior anticancer performance by the synergism of ferroptosis and immunomodulation.

**Anticancer Performance of FDPM Nanoparticles *In Vivo*.** Encouraged by the superior antitumor performance and immunomodulation of the synthesized nanoparticles in this study, we also conducted an antitumor experiment in a human cell line-derived tumor model. All HOS tumor-bearing nude mice with a tumor size of  $\sim 100 \text{ mm}^3$  were randomly divided into five groups and then treated with PBS, FDPM, FDPM + Light, and FDPM + Light + Fer-1 (Figure 9A). PBS and FDPM nanoparticles were intravenously injected, whereas Fer-1 (5 mg/kg) was intratumorally (i.t.) delivered. After 8 h, white light irradiation was conducted on all laser groups for 15 min ( $100 \text{ W/cm}^2$ ). After treatment for 24 h, each group was carefully assessed for their MDA and GSH levels ( $n = 5$ ).<sup>9</sup> Relative to that in the PBS group, MDA generation and GSH depletion were markedly increased in the FDPM + Light group; meanwhile, additional administration of Fer-1 markedly resecured MDA generation and GSH depletion (Figures 9B,C). These results demonstrated that with laser irradiation, FDPM could lead to serious oxidation stress damage, which was consistent with the cell experiments.

Subsequently, we further confirmed the FDPM + Light-induced ferroptosis in the HOS tumor model. All tumor-bearing nude mice with a tumor size of  $\sim 100 \text{ mm}^3$  were randomly divided into five groups ( $n = 5$ ). After different treatments for 3 days, the tumors were collected for histological analyses (H&E, Prussian blue, LPO staining, and IHC staining). Compared with those in the PBS and other experimental groups, the amount of LPO was substantially increased and the positive area of Prussian blue staining was evidently observed in the FDPM + Light group, which could be alleviated by administering additional Fer-1 (Figure 9D). Further, a significant inhibitory effect of Nrf2 was observed in the FDPM + Light group compared with that in the PBS control (Figure 9D), which was consistent with the results of the K7M2 tumor model. In

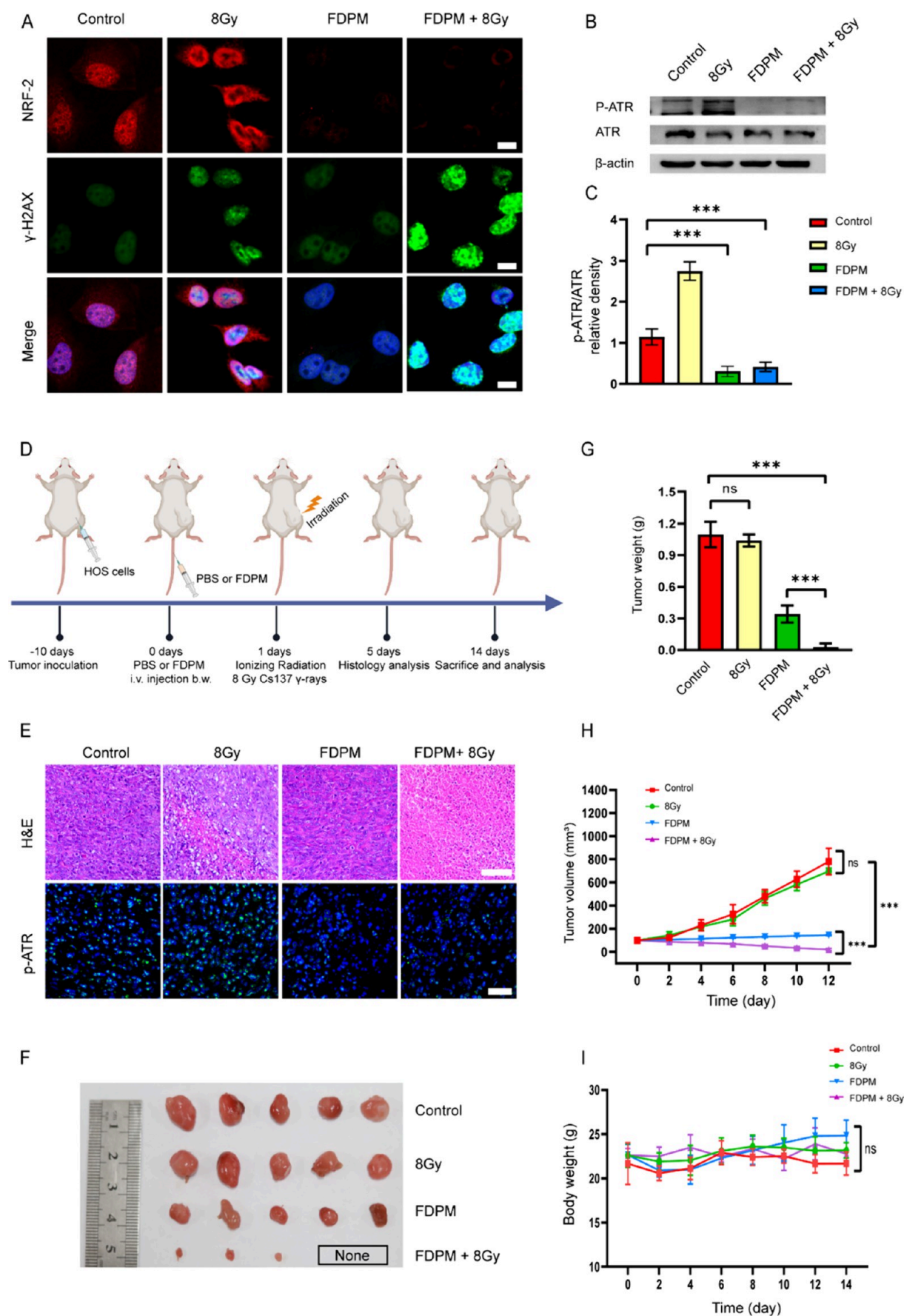


**Figure 10.** FDPM nanoparticles inhibit the activation of the Nrf2-ATR signaling pathway and promote sensitivity to DNA repair. (A) CLSM images of immunofluorescence staining showing Nrf2 expression and  $\gamma$ -H2AX proteins after different treatments. Scale bar: 20 nm. (B, C) Total and

Figure 10. continued

phosphorylated protein levels of ATR analyzed using Western blots in HOS cells after different treatments ( $n = 3$ ). (D) Schematic of the strategy of HOS tumor-bearing nude mice for different treatments. Twenty hours postinjection, all IR groups were exposed to 8 Gy Cs137  $\gamma$ -rays for 6 h. (E) Histological evaluation of tumor tissues from each group after different treatments ( $n = 5$ ). Assessment of tissue damage by H&E staining. Scale bar: 100  $\mu\text{m}$ . Immunofluorescence staining of p-ATR to assess the phosphorylation level of ATR in tumors by using different treatments. Scale bar: 50  $\mu\text{m}$ . (F, G, H, and I) Tumor size (F, G), tumor growth (H) curves, and body weight (I) of HOS tumor-bearing nude mice recorded every 2 days after different treatments ( $n = 5$ ). Data are presented as mean  $\pm$  SEM and were analyzed using unpaired two-sided Student's  $t$  test (ns: no significance,  $*p < 0.05$ ,  $**p < 0.01$ ,  $***p < 0.001$ ).

In addition, severe tissue damage and looseness were observed in the FDPM and FDPM + Light groups, whereas compactness without obvious dying cells was found in the other groups, as determined by H&E staining (Figure 9D). The surface-exposed CRT facilitates tumor antigen presentation and tumor-specific CTLs responses.<sup>34</sup> In our study, the surface CRT of the dying HOS cells was markedly upregulated only in the FDPM + Light group (Figure 9D). Comprehensively, we confirmed that PDT induced by FDPM nanoparticles exposed to laser irradiation could trigger ICD to HOS cells and release DAMPs into the TME.

Last, we investigated the potential anticancer effect of the FDPM-induced strategy based on ferroptosis. All tumor-bearing nude mice with a tumor size of  $\sim 100 \text{ mm}^3$  were randomly divided into five groups ( $n = 8$ ). The tumor size and the body weight were recorded within 20 days, and the tumor weight was measured at the 20 days.<sup>9</sup> The antitumor effect was significant in the FDPM group and was even greater in the FDPM + Light group compared with the PBS and FDP groups. In addition, this antitumor effect could be resecured by the additional administration of Fer-1 (Figure 9E–G). Meanwhile, no significant difference in body weight was found between the groups (Figure S8).

**Effect of FDPM Nanoparticles on Radiosensitivity.** MDR remains a significant obstacle to successful chemotherapy treatment for osteosarcoma patients.<sup>3</sup> One of the most important mechanisms by which osteosarcoma remained resistant to radiotherapy or chemotherapy is an increase in the ability of intracellular DNA damage response (DDR).<sup>51,52</sup> DDR is a signal transduction pathway involved in protecting cells against DNA damage caused by endogenous and exogenous factors such as chemotherapy agents, ionizing radiation (IR), and replication fork stress.<sup>53,54</sup> Previous studies have demonstrated that Nrf-2 plays an important role in DDR against DNA damage via numerous mechanisms such as the antioxidant and ATR pathways,<sup>54–56</sup> as demonstrated in Figure 3D. Considering the good targeting properties, excellent ROS generation ability, and significant Nrf2 inhibition effect of FDPM nanoparticles, we hypothesized that the efficiency of radiotherapy could be significantly improved by FDPM nanoparticles. Using  $\gamma$ -H2AX as a DNA damage marker, we initially found that HOS cells exhibited only slight DNA damage through overexpression and enhanced the signal transduction of Nrf-2 under IR. Combined with IR treatment, treatment with FDPM nanoparticles could significantly inhibit Nrf2 expression and enhance P- $\gamma$ H2AX expression in HOS cells (Figure 10A). Previous studies have shown that phosphoinositide 3-kinase-related protein kinases, including ataxia-telangiectasia mutated and ATR protein kinases, are the master regulators of DDR.<sup>57–59</sup> Nrf2, as the master responder to oxidative and electrophilic stresses, was recruited to chromatin where it phosphorylated ATR and activated the ATR–CHK1–CDC2 signaling pathway in response to DNA damage,<sup>54,56</sup> as demonstrated in Figure 3D. In the

present study, we confirmed that FDPM nanoparticles could inhibit ATR phosphorylation (Figure 10B,C). To further explore whether FDPM nanoparticles could inhibit the Nrf2–ATR signaling pathway and regulate radiosensitivity *in vivo*, we conducted animal experiments. All tumor-bearing nude mice with a tumor size of  $\sim 100 \text{ mm}^3$  were randomly divided into four groups ( $n = 5$ ) and then treated with PBS, 8 Gy, FDPM, and FDPM + 8 Gy (Figure 10D). Both the PBS and FDPM nanoparticles were intravenously injected; after 24 h, all IR groups were exposed to 8 Gy Cs137  $\gamma$ -rays for 6 h.<sup>54</sup> After different treatments for 5 days, the tumors were collected for histological analysis, including H&E staining and IF staining. The H&E results indicated that compared with the PBS and FDPM groups, the group exposed to 8 Gy only showed slight tissue damage, and the FDPM + 8 Gy group displayed serious tissue damage (Figure 10E). IF staining also demonstrated that the phosphorylation level of ATR was severely inhibited in the FDPM and FDPM + 8 Gy groups (Figure 10E), which was consistent with cell experiments *in vitro*. Subsequently, we carefully assessed the antitumor effect of FDPM exposed to IR spectroscopy *in vivo*. All tumor-bearing nude mice with a tumor size of  $\sim 100 \text{ mm}^3$  were randomly divided into four groups ( $n = 5$ ). The tumor size and the body weight were recorded within 14 days, and the tumor weight was measured at the 14 days.<sup>54</sup> A significant reduction in the tumor size was observed in the FDPM + 8 Gy group (Figures 10F–H), whereas no significant difference in body weight was found between the groups (Figure 10I). The combined results showed that the FDPM nanoparticles could effectively improve the radiosensitivity of osteosarcoma through activation of the Nrf2–ATR signaling pathway *in vitro* and *in vivo*.

**Biosafety and Toxicity of FDPM Nanoparticles.** We carefully investigated the potential toxic effects of FDPM nanoparticles *in vivo*. After 7 days with various treatments in the HOS tumor-bearing model, blood in all groups was systematically collected for blood chemistry and serum biochemistry analyses.<sup>22</sup> No significant differences in all serum biochemistry and blood chemistry indicators were found between the control group and the treatment group (Figure S9). At the end of the observations, major organs, including the heart, liver, spleen, lung, and kidney were harvested for H&E staining assays. No obvious pathological abnormalities were observed in major organ sections, and variations in the average body weight of mice were negligible in all groups (Figure S10). These results demonstrate the good biocompatibility of synthesized FDPM nanoparticles *in vivo*.

## CONCLUSIONS

We found that cancer cells could avoid lethal ferroptosis caused by oxidation stress derived from  $\text{Fe}_3\text{O}_4$  nanoparticles by the feedback activation of the Nrf2 pathway. On the basis of this finding, DHJS could reverse Nrf2 overexpression as well as enhance the sensitivity of ferroptosis induced by  $\text{Fe}_3\text{O}_4$

nanoparticles. Therefore, we created a HOS and RBC hybrid biomimetic membrane (HRM) and then camouflaged the PLGA nanomicrospheres-loaded  $\text{Fe}_3\text{O}_4$  and DHJS as FDPM nanoparticles. The nanoparticles exhibited the extension of blood circulation life and enhanced the homologous targeting ability owing to the inherit properties derived from HRM coating. Our data demonstrated that it could synergize with  $\text{Fe}_3\text{O}_4$  nanoparticles to trigger lethal ferroptosis in cancer cells. Moreover, FDPM nanoparticles induced macrophage M1 polarization and promoted the release of DAMPs into TME. As shown by the different animal models, FDPM nanoparticles exhibited excellent antitumor performance via ferroptosis and immunomodulation synergism. Our work has major implications for the therapeutic applications of  $\text{Fe}_3\text{O}_4$  nanoparticles. Meanwhile, we developed a novel practical strategy for enhanced antitumor ferroptosis-immunotherapy.

## MATERIALS AND METHODS

**Materials.** Ethanol was obtained from the China National Pharmaceutical Group Corporation. Poly(-lactic-co-glycolide) (poly (lactic-co-glycolic acid) (PLGA), Mw 7000–17,000, lactide/glycolide 50:50), oleic acid (OA), oleylamine, dichloromethane, ferric acetylacetonate ( $\text{Fe}(\text{acac})_3$ ), 1-octadecanol, and diphenyl ether were purchased from Aladdin Biochemical Technology Co., Ltd. Propidium iodide (PI), Membrane and Cytosol Protein Extraction Kit, Cell Counting Kit-8 (CCK8), 1,1'-dioctadecyl-3,3,3',3'-tetramethylindocarbocyanine perchlorate (DiI), and 3,3'-dioctadecyloxycarbocyanine perchlorate (DiO) were purchased from Beyotime Biotechnology. The antibodies used for Western blot and flow cytometry analysis are shown in Table S1. The mouse macrophage colony-stimulating factor (M-CSF) was purchased from PeproTech. All reagents were directly used without purification.

**Characterization.** TEM images were obtained from a HITACHI HT7700 operated at 80 kV. Hydrodynamic diameter and  $\zeta$  potential were measured with a Zetasizer NanoZS90 (Malvern). Absorption spectra were measured by using a UV-vis spectrophotometer (Agilent Technologies). Cell membrane fusion of HOS and RBC was detected by a confocal fluorescence microscope (CLSM, Leica LAS X). Flow cytometric analysis was performed by a flow cytometer (FCM, Beckman, cytoflex S).

**Preparation of  $\text{Fe}_3\text{O}_4$  and FDP Nanoparticles.** OA-coated  $\text{Fe}_3\text{O}_4$  nanoparticles were prepared according to previous reports.<sup>60,61</sup> Briefly, 1.41 g (4 mmol) of  $\text{Fe}(\text{acac})_3$ , 3.39 g (12 mmol) of oleic acid, 3.21 g (12 mmol) of oleylamine, and 2.70 g (10 mmol) of 1-octadecanol were dissolved in 40 mL of diphenyl ether. After being purged with argon for 30 min, the resultant solution was heated to 260 °C for 30 min under an oxygen-free environment to generate OA-coated  $\text{Fe}_3\text{O}_4$ . After that, the reaction mixture was cooled to room temperature. Then, the resultant nanoparticles were precipitated by ethanol, collected by centrifugation (6,000 rpm, 8 min), washed with ethanol three times, and finally redispersed in dichloromethane for further experiments.

To prepare  $\text{Fe}_3\text{O}_4$ -DHJS nanoparticles, a single emulsion method was applied. Briefly, 10 mg PLGA, 50  $\mu\text{L}$   $\text{Fe}_3\text{O}_4$  NPs ( $\text{Fe}^{3+}$  4.8 mg/mL), and 41.5  $\mu\text{g}$  DHJS were dissolved in 0.5 mL of dichloromethane. Three milliliters of 2% (w/v) PVA (poly(vinyl alcohol)) aqueous solution was added into the above solution and sonicated (Sonics & Materials, Inc.) at 30% power and pulsing (Ton = 3 s, Toff = 7 s) for 20 rounds on ice followed by magnetically stirring at 600 rpm overnight to evaporate the organic solvent. The nanoparticles were collected by centrifuging at 10,000 rpm for 10 min and washed twice with deionized water to remove PVA. PLGA-NPs loaded with  $\text{Fe}_3\text{O}_4$  were fabricated in a similar way as that for the  $\text{Fe}_3\text{O}_4$ -DHJS NPs.

**Preparation of the HOS Cell Membrane and RBC Membrane.** To obtain the HOS-M, cells cultured in 175  $\text{cm}^2$  cell culture flasks were collected with a cell scraper followed by centrifugation at 300g for 5 min and washing twice with PBS. Then, the obtained cell pellets were added into hypotonic lysing buffer containing the membrane protein extraction reagent and protease inhibitor of phenylmethanesulfonyl

fluoride (PMSF) according to the manufacturer's instructions (Beyotime Institute of Biotechnology). After treatment in an ice bath for 15 min, the cell lysing buffer was further processed with sonication (Sonics & Materials, Inc.) at 15% power and pulsing (Ton = 3 s, Toff = 7 s) for five rounds on ice. After sonication, the solution was centrifuged at 700g for 10 min, and the supernatant was carefully collected and further centrifuged at 14,000 rpm for 20 min at 4 °C. Then, the membrane material derived as described above was physically extruded through an 800 nm polycarbonate membrane for 15 passes to create the HOS-M material. The obtained HOS-M was resuspended in PBS or deionized water for further use.

To obtain RBC-M, the whole blood from BALB/c mouse was centrifuged at 3000 rpm for 10 min to remove plasma, platelets, and white blood cells and washed once with PBS. Then, RBC-Ms were obtained according to a previously reported hypotonic treatment.<sup>22</sup> Briefly, the volume ratio of RBCs to deionized water containing EDTA was 1:50, and the mixed solution was kept in an ice bath for 15 min followed by centrifugation at 700g for 5 min to remove residual white blood cells. The supernatant was carefully collected and centrifuged at 14,000 rpm for 20 min at 4 °C. Then, RBC-M pellets were redispersed in deionized water and repeatedly centrifuged to remove hemoglobin until the supernatant was colorless. Then, the membrane material derived as described above was physically extruded through an 800 nm polycarbonate membrane for 15 passes to create the RBC-M material. The obtained RBC-M was resuspended in PBS or deionized water and stored at 4 °C for further use.

**Preparation and Characterization of the HOS-RBC Hybrid Membrane.** The membrane protein concentrations of HOS-M and RBC-M were detected by a BCA protein kit (Beyotime Institute of Biotechnology). The DiI-labeled RBC-M (excitation/emission = 549/565 nm) was added to DiO-labeled HOS-M (excitation/emission = 484/501 nm) at the membrane protein weight ratio of 1:1 followed by a mixture at 37 °C for 10 min to facilitate membrane fusion. The fusion results were detected by a fluorescence microscope.

**Preparation of the K7M2-RBC Hybrid Membrane.** Taking into account that HOS is a human-derived osteosarcoma cell line and due to the limitations in utilizing the HOS tumor-bearing nude mice for immunological analyses, we reconstructed the hybrid cell membrane system (KRM) using RBC and the mouse-derived osteosarcoma cell line K7M2. The hybrid KRM system was constructed in the same way as the HRM system described above.

**Preparation of FDPM Nanoparticles.** HOS-M solution (5 mL, 1 mg/mL) was mixed with RBC-M solution (5 mL, 1 mg/mL) at a membrane protein weight ratio of 1:1 followed by mixture at 37 °C for 10 min to obtain HRM. Then, to form FDPM nanoparticles, the hybrid membrane (10 mL, 1 mg/mL) was coated onto  $\text{Fe}_3\text{O}_4$ -DHJS@PLGA nanoparticles (10 mL, 1 mg/mL) by coextruding cell membrane and cores through a 400 nm polycarbonate membrane for 15 passes. The obtained FDPM nanoparticles were stored under 4 °C for further use.

The loading efficiency and loading capacity of  $\text{Fe}_3\text{O}_4$  or DHJS by PLGA were calculated as follow:

Loading efficiency (LE) = weight of loaded A/weight of added A 100%

Loading capacity (LC) = weight of loaded A/weight of PLGA nanoparticle 100%

**Preparation of FDKM Nanoparticles.** Following the method described above, we constructed FDKM nanoparticles (Fe concentration at 10  $\mu\text{g}/\text{mL}$  and DHJS concentration at 2  $\mu\text{M}$ ) for immunological analysis using K7M2-M, RBC-M, and FDP nanoparticles.

**Cytotoxicity Study of DHJS Nanoparticles or FDPM Nanoparticles.** The cytotoxicity of these nanoparticles to HOS cells was measured by using a CCK-8 assay kit (Dojindo). Briefly, HOS cells were seeded in 96-well plates at a density of  $5 \times 10^3$  per well for 24 h. Then, DHJS nanoparticles or FDPM nanoparticles (DHJS concentration at 0, 1, 2, 4, and 8  $\mu\text{M}$ ) were added to HOS cells. When the incubation time reached 4 h, the NPs + Light group was irradiated with a white-light lamp (8.5  $\text{mW}/\text{cm}^2$ ) for 30 min. After incubation for 24 h followed by washing three times with PBS to remove uncombined nanoparticles, the supernatant was removed, and 100  $\mu\text{L}$  of fresh

medium containing 10  $\mu\text{L}$  of the CCK-8 reagent was added and incubated for another 2 h at 37  $^{\circ}\text{C}$  in the dark. The absorbance was detected at 450 nm on a microplate reader (BioTek, ELx808). In addition, HOS, ID8, MC3T3, and RAW 264.7 cells were also incubated with FDPM nanoparticles (DHJS concentration at 2  $\mu\text{M}$  and white light: 8.5  $\text{mW}/\text{cm}^2$ , 30 min) for 24 h to further assess the cytotoxicity of nanoparticles to other types of cells.

**Homologous Targeting Study of FDPM.** HOS, ID8, MC3T3, and RAW 264.7 cells were seeded in 12-well plates at a density of  $5 \times 10^4$  cells per well and cultured for 24 h. Fresh media containing FDPM nanoparticles (Fe concentration of 10  $\mu\text{g}/\text{mL}$ ) were added to each kind of cell. After incubation for 1 h, 2 or 4 h, these cells were washed three times with PBS, and the fluorescence signal was detected using CLSM and FCM (DHJS:  $\lambda_{\text{ex}} = 640 \text{ nm}$ ,  $\lambda_{\text{em}} = 697 \text{ nm}$ ).

**Cell Lines and Cell Culture.** Osteosarcoma cell lines HOS and K7M2 were purchased from the American Type Culture Collection (ATCC, Manassas, VA, USA). The ID8 cell line was provided by K. Roby (Department of Anatomy and Cell Biology, University of Kansas). RAW 264.7 and MC3TC cell lines were provided by the Cell Bank of the Chinese Academy of Sciences (Shanghai, China). All of the cell lines were cultured in Dulbecco's modified Eagle medium (DMEM) (Gibco) supplemented with 10% fetal bovine serum (FBS), 100 U/mL penicillin, and 100  $\mu\text{g}/\text{mL}$  streptomycin. The cells were maintained at 37  $^{\circ}\text{C}$  in a humidified atmosphere of 5%  $\text{CO}_2$ .

**Animal Experiment.** All animal procedures carried out in our study were in compliance with the Guide for the Care and Use of Laboratory Animals by the US National Institutes of Health (NIH Publication, revised in 2011), and all intervention procedures on the mice were approved by the Animal Care and Use Committee of Tongji Medical College (TJH-201903021). The 8 week old male C57BL/6 mice, 6 week old male BALB/c nude mice, and female BALB/c mice were purchased from Beijing HFK Bioscience Co., Ltd., and housed in specific pathogen-free conditions. To establish the subcutaneous xenograft tumor model,  $1 \times 10^6$  HOS cells and  $5 \times 10^6$  K7M2 cells were injected into the axilla of BALB/c nude mice and flank of BALB/c mice, respectively. Then, HOS tumor-bearing nude mice or K7M2 tumor-bearing mice with a tumor size of  $\sim 100 \text{ mm}^3$  were randomly divided into different groups. After 8 h of nanoparticle injection, all white-light groups were irradiated with 100  $\text{W}/\text{cm}^2$  for 15 min, and all IR groups were exposed to 8 Gy Cs137  $\gamma$ -rays. The tumor size was measured every 2 days or 3 days with a caliper, and the tumor volume was calculated as volume ( $\text{mm}^3$ ) =  $0.5 \times \text{width}^2 \times \text{length}$ . All animal experiments were performed when the tumor volume reached a value of approximately 100  $\text{mm}^3$ .

**Adenoviral Transduction.** Adenoviruses carrying shRNA-targeting human Nrf2 and control adenoviruses were purchased from Vigene Biosciences (Rockville, MD, USA). The shRNA sequence was as follows: 5'-CCGGGCTCCTACTGTGATGTGAAATCTCGA-GATTCACATCACAGTAGGAGCTTTT-3'. For adenoviral transfection, cells were plated 1 day prior to infection, cultured overnight to reach 70–80% confluency, and then incubated with adenoviral particles (50 particles per cell) for 12 h. Knockdown effects were confirmed by Western blot.

**Bone-Marrow-Derived Macrophage Isolation.** Bone-marrow-derived macrophages (BMMs) were isolated from the long bones of 8 week old male C57BL/6 mice. Briefly, the tibias and femurs were separated, and then the bone marrow cells were flushed out from marrow cavities. The cells were cultured in an  $\alpha$ -MEM medium containing 10% FBS and M-CSF (30  $\text{ng}/\text{mL}$ ) for 16 h. Next, the medium containing floating cells was transferred to a new culture dish, and after 2 days, the adherent cells were considered as BMMs for further use.

**RNA Isolation and Quantitative PCR Analysis.** Total RNA was extracted from culture cells using TRIzol reagent (Invitrogen, Carlsbad, CA, USA) according to the manufacturer's instructions and then subjected to cDNA synthesis using HiScript Q RT SuperMix (Vazyme Biotech, Nanjing, China). Real-time PCR was performed using SYBR Green Master Mix (Invitrogen), and the PCR was monitored using the CFX Connect system (Bio-Rad). The primer sets used were as shown in Table S1.

**Western Blotting Analysis.** Total protein was extracted from cultured cells using RIPA buffer supplemented with 1% proteinase inhibitor and 1% phosphotransferase inhibitor (Boster Biotechnology). Proteins were resolved and separated by 10% SDS-PAGE gel electrophoresis and then transferred onto PVDF membranes (Millipore). After being blocked with 5% BSA for 1 h, the membranes were incubated with indicated primary antibodies at 4  $^{\circ}\text{C}$  overnight and secondary antibodies at 25  $^{\circ}\text{C}$  for 1 h with gentle shaking. The antibodies used for Western blot are listed in Table S1. The signals were detected by using an electrochemical luminescence reagent (Thermo Scientific).

**Quantification of HMGB1 and ATP.** For the quantification of ATP release, the cells were incubated in a medium with 2% FBS for 24 h. After treatment, supernatants were collected and centrifuged at 15,000 rpm at 4  $^{\circ}\text{C}$  for 3 min for further assay. For the quantification of HMGB1 release, the supernatants were also collected, cleared by centrifugation, and frozen at  $-20 \text{ }^{\circ}\text{C}$ . All assays were performed in accordance with the respective manufacturers' instructions by ELISA kits (IBL-Hamburg). Luminescence was measured on a Tecan Spark 20 M multimode microplate reader.

**Measurement of MDA and GSH.** The content of MDA in culture cells and tumor tissue was measured by using a lipid peroxidation MDA assay kit (Beyotime). MDA level was determined by a Synergy HT multimode microplate reader (BioTek, Winooski, Vermont, USA) at 535 nm and normalized to protein concentration. The levels of total and oxidized glutathione were also measured by using the GSH/GSSG assay kit (Beyotime). The content of GSH was determined with a Synergy HT multimode microplate reader (BioTek, Winooski, Vermont, USA) at 412 nm. The level of reduced GSH was obtained by subtracting GSSG from the total glutathione and normalizing the level to protein concentration.

**Measurement of Cytosolic ROS and Lipid-ROS.** Intracellular cytosolic ROS was measured by using an ROS assay kit (Beyotime). In brief, after treatment, cells were collected, and the DCFH-DA probe was loaded. The cells were incubated with DCFH-DA at 37  $^{\circ}\text{C}$  for 20 min protected from light, then washed three times with serum-free medium, and finally visualized using CLSM or FCM.

Generation of lipid ROS was detected by using a BODIPY 581/591 C11 sensor (Thermo Fisher). In brief, the cells were then incubated with a BODIPY 581/591 C11 staining solution for 40 min at 37  $^{\circ}\text{C}$  protected from light. After being stained, the cells were washed three times and immediately imaged by CLSM or FCM.

**Total Iron and Ferrous Detection.** To detect intracellular  $\text{Fe}^{2+}$ , Ferro-Orange (DojinDo, Japan) fluorescent probes were used according to the manufacturer's protocol. In brief, the culture cells were treated with 1  $\mu\text{mol}/\text{L}$  FerroOrange with Hank's balanced salt solution (HBSS) (Gibco, USA) for 30 min at 37  $^{\circ}\text{C}$ . The cells were observed under CLSM.

For qualification of the  $\text{Fe}^{2+}$  content, the relative  $\text{Fe}^{2+}$  concentration was assessed using an Iron Assay Kit (Sigma-Aldrich, MAK025). In briefly, the samples were collected and processed following the manufacturer's manual. The absorbance at 593 nm was measured using a microplate reader, and the sample concentration was counted based on the standard curve.

For qualification of total iron content, the amount of total iron was determined by an atomic absorption spectrometer (AAS, Analytik Jena, Germany). In brief, the samples for iron quantification were heat-disrupted with 500  $\mu\text{L}$  of  $\text{HNO}_3$  at 70  $^{\circ}\text{C}$  for 2 h. The samples were analyzed by AAS, and the total iron content was normalized to protein concentration.

**Cellular Immunofluorescence Assay.** The cells were fixed with 2% paraformaldehyde and incubated with primary antibodies in PBS with 1% bovine serum albumin overnight at 4  $^{\circ}\text{C}$ . After washing and application of secondary antibodies, sections were protected with coverslips with an antifading mounting medium sealed with nail polish. Immunofluorescence images were acquired by using CLSM.

**Histochemical Analysis.** After treatments, the tumor-bearing mice were euthanized, and the tumors were harvested for the histochemical staining. The tumor tissues were fixed in 4% paraformaldehyde overnight, embedded, and sliced into 5  $\mu\text{m}$  thick sections for H&E,

Prussian blue, LPO, anti-Nrf2, anti-CRT, anti-CD80, and anti-CD206 IHC staining (Table S2). These images of stained plates were obtained using an EVOS scanner (Thermo Fisher Scientific)

**Coculture System.** Migration assays of macrophages were conducted by using Transwell inserts (6.5 mm diameter, 8.0  $\mu\text{m}$  pore size). Briefly,  $2 \times 10^4$  BMM cells were seeded on the upper chamber with 200  $\mu\text{L}$  of serum-free DMEM. The K7M2 cells were then cocultured with the BMM cells at a ratio of 1:1 for 24 h before treatments, and the lower chamber was filled with 700  $\mu\text{L}$  of serum-free DMEM.

After incubation for 24 h, the insets were pretreated, and the migrated cells were stained with 0.05% crystal violet. The culture medium was retrieved from the coculture system, and levels of hydroxyl radical and hydrogen peroxide were determined using colorimetric hydrogen peroxide and 3'-(*p*-hydroxyphenyl) fluorescein (HPF) detection kits, respectively. Briefly, the hydroxyl radical was measured by incubating the coculture medium with HPF (Thermo Fisher Scientific) at a concentration of 10 mM for 30 min at 37  $^\circ\text{C}$  and measuring HPF fluorescence at an emission wavelength of 515 nm (excitation wavelength 490 nm). The hydrogen peroxide in coculture media was determined by incubating with a hydrogen peroxide colorimetric detection kit for 30 min at 25  $^\circ\text{C}$  (Enzo Life Science), and the resultant absorbance was measured at 550 nm.

**Flow Cytometry Analysis.** Mice were euthanized with ketamine (100 mg/kg) and xylazine (10 mg/kg) intraperitoneally. In all tumors, draining lymph nodes were collected and taken into ice-cold PBS. The tissue samples were cut into pieces with a razor blade, washed, and weighed for further use. Tumor debris were incubated for 30 min at 37  $^\circ\text{C}$  in DMEM with 2.0 mg/mL Collagenase A (Roche) and 50 U/mL DNase I (Roche) and then filtered through 70  $\mu\text{m}$  nylon strainers (BD Biosciences) for the preparation of single cell suspensions. The single cell suspensions of draining lymph node samples were also prepared by grinding and filtering. Thereafter, cells were incubated for 15 min with the Fc Receptor Binding Inhibitor (eBioscience, USA) diluted 1/10 in PBS on ice. Fluorochrome-conjugated primary antibodies were added to single-cell suspensions, and the suspensions were incubated for 30 min. The antibodies used for flow cytometry (FCM) analysis are listed in Table S1. All antibodies and secondary reagents were titrated to determine the optimal concentrations. For gating, fluorescence minus one control was used. Tumor macrophages were identified as CD45<sup>+</sup> CD11b<sup>+</sup> F4/80<sup>+</sup> cell subsets, wherein M1 macrophages were defined as CD80<sup>+</sup> CD206<sup>-</sup> cell and M2 macrophages were CD206<sup>+</sup> cells. Tumor CD4<sup>+</sup> T cells were defined as CD45<sup>+</sup> CD3<sup>+</sup> CD4<sup>+</sup> cells, and CTLs were defined as CD45<sup>+</sup> CD3<sup>+</sup> CD8<sup>+</sup> cells. The CTLs in LNs were defined as CD3<sup>+</sup> CD8<sup>+</sup> cell subsets, and matured DCs were identified as CD11c<sup>+</sup> CD80<sup>+</sup> CD86<sup>+</sup> cells. The data of FCM were acquired using FACSDiva software version 9.0 and analyzed with FlowJo\_v10 (TreeStar) software.

**TEM.** The culture cells were collected, fixed with 2.5% electron microscopy-grade glutaraldehyde at 4  $^\circ\text{C}$  overnight, and stained with 4% osmium tetroxide at 25  $^\circ\text{C}$  for 30 min. Subsequently, the cells were dehydrated in gradient ethanol (30–100%) at room temperature, embedded in epoxy resin, and cured at 60  $^\circ\text{C}$  for 48 h. Ultrathin cell sections (80 nm) were prepared, stained with 5% uranyl acetate and 2% lead citrate, and observed under a Hitachi TEM system (Hitachi, HT7800).

**Pharmacokinetics and Biodistribution of Nanoparticles.** The 6 week old male BALB/c nude mice with HOS tumor were randomly divided into three groups ( $n = 8$ ) and received a tail vein injection of FDP and FDPM nanoparticles, and PBS was injected as a background for Fe content detection. Blood was collected for biodistribution analysis at 1, 2, 4, 8, 16, and 24 h. Major organs (heart, liver, spleen, lung, and kidney) and tumor tissues were gathered, weighed, and dissolved in chloroazotic acid. Fe contents in blood samples were measured by AAS. Nanoparticle concentrations in blood, organs, and tumors were expressed as a percentage of the injected nanoparticle dose per gram of tissue (% ID/g).

**Biosafety and Toxicity of Nanoparticles.** At day 7 after the various treatments, the mice were anesthetized, and blood was collected for serum biochemistry and blood chemistry analyses. At the end of

observations, the major organs (heart, liver, spleen, lung, and kidney) were harvested for H&E staining.

## ■ ASSOCIATED CONTENT

### Supporting Information

The Supporting Information is available free of charge at <https://pubs.acs.org/doi/10.1021/acsami.3c07379>.

Cell viability; loading capacity of Fe<sub>3</sub>O<sub>4</sub> and DHJS; long-term stability of FDPM; biodistribution of FDP@RBC-M, FDP@HOS-M, and FDPM; Western blot analysis of Fe metabolism, Nrf2-related pathway, and ferroptosis pathway; pharmacokinetics of FDP@RBC-M, FDP@K7M2-M, and FDKM; body weight curves; biosafety evaluation of FDPM nanoparticles; and primers and antibodies used in this study (PDF)

## ■ AUTHOR INFORMATION

### Corresponding Authors

**Jiaqiang Xiong** – Department of Obstetrics and Gynecology, Zhongnan Hospital of Wuhan University, Wuhan 430071, China; [orcid.org/0000-0002-8490-6613](https://orcid.org/0000-0002-8490-6613); Email: [jiaqiangxiong@163.com](mailto:jiaqiangxiong@163.com)

**Yi Liu** – Non-power Nuclear Technology Collaborative Innovation Center, School of Nuclear Technology and Chemistry & Biology, Hubei University of Science and Technology, Xianning 437100, P. R. China; State Key Laboratory of Separation Membrane and Membrane Process, School of Chemistry and Chemical Engineering & School of Environmental Science and Engineering, Tiangong University, Tianjin 300387, China; [orcid.org/0000-0001-7626-0026](https://orcid.org/0000-0001-7626-0026); Email: [yiliuchem@whu.edu.cn](mailto:yiliuchem@whu.edu.cn)

**Feng Li** – Department of Orthopedics, Tongji Hospital, Tongji Medical College, Huazhong University of Science and Technology, Wuhan 430015, P. R. China; Email: [lifengmd@hust.edu.cn](mailto:lifengmd@hust.edu.cn)

### Authors

**Kaixu Yu** – Department of Orthopedics, Tongji Hospital, Tongji Medical College, Huazhong University of Science and Technology, Wuhan 430015, P. R. China; [orcid.org/0000-0002-4348-3239](https://orcid.org/0000-0002-4348-3239)

**Ying Chen** – Department of Obstetrics and Gynecology, Tongji Hospital, Tongji Medical College, Huazhong University of Science and Technology, Wuhan 430015, P. R. China

**Lu Zhang** – Non-power Nuclear Technology Collaborative Innovation Center, School of Nuclear Technology and Chemistry & Biology, Hubei University of Science and Technology, Xianning 437100, P. R. China

**Yongqiang Zheng** – State Key Laboratory of Oncology in South China, Sun Yat-sen University Cancer Center, Sun Yat-sen University, Guangzhou 510060, P. R. China

**Jinlin Chen** – Department of Orthopedics, Tongji Hospital, Tongji Medical College, Huazhong University of Science and Technology, Wuhan 430015, P. R. China

**Zhenhua Wang** – Frontiers Science Center for Flexible Electronics, Xi'an Institute of Flexible Electronics (IFE) & Xi'an Institute of Biomedical Materials and Engineering (IBME), Northwestern Polytechnical University, Xi'an 710072, P. R. China; [orcid.org/0000-0002-9028-6799](https://orcid.org/0000-0002-9028-6799)

**Xiaogang Yu** – State Key Laboratory of Structure Analysis for Industrial Equipment, Department of Engineering Mechanics, Dalian University of Technology, Dalian 116024, P. R. China

**Kehan Song** – Department of Orthopedics, Tongji Hospital, Tongji Medical College, Huazhong University of Science and Technology, Wuhan 430015, P. R. China

**Yimin Dong** – Department of Orthopedics, Tongji Hospital, Tongji Medical College, Huazhong University of Science and Technology, Wuhan 430015, P. R. China

**Fanxiu Xiong** – Department of Epidemiology and Biostatistics, University of California, San Francisco, California 94199, United States

**Zijian Dong** – Department of Orthopedics, Tongji Hospital, Tongji Medical College, Huazhong University of Science and Technology, Wuhan 430015, P. R. China

**Hao Zhu** – Department of Orthopedics, Tongji Hospital, Tongji Medical College, Huazhong University of Science and Technology, Wuhan 430015, P. R. China

**Gaohong Sheng** – Department of Orthopedics, Tongji Hospital, Tongji Medical College, Huazhong University of Science and Technology, Wuhan 430015, P. R. China

**Meipeng Zhu** – Department of Orthopedics, Tongji Hospital, Tongji Medical College, Huazhong University of Science and Technology, Wuhan 430015, P. R. China

**Xi Yuan** – Department of Orthopedics, Tongji Hospital, Tongji Medical College, Huazhong University of Science and Technology, Wuhan 430015, P. R. China

**Hanfeng Guan** – Department of Orthopedics, Tongji Hospital, Tongji Medical College, Huazhong University of Science and Technology, Wuhan 430015, P. R. China

Complete contact information is available at:  
<https://pubs.acs.org/10.1021/acsami.3c07379>

## Author Contributions

The manuscript was written through the contributions of all authors. All authors have given approval to the final version of the manuscript.

## Notes

The authors declare no competing financial interest.

## ACKNOWLEDGMENTS

This work was supported by grants from the National Nature Science Foundation of China (82072500 and 81974351), and Science and Technology Plans of Tianjin (22ZYJDS00070).

## REFERENCES

- (1) Beird, H. C.; Bielack, S. S.; Flanagan, A. M.; Gill, J.; Heymann, D.; Janeway, K. A.; Livingston, J. A.; Roberts, R. D.; Strauss, S. J.; Gorlick, R. Osteosarcoma. *Nat. Rev. Dis. Primers* **2022**, *8* (1), 77.
- (2) Zhu, J.; Simayi, N.; Wan, R.; Huang, W. CAR T Targets and Microenvironmental Barriers of Osteosarcoma. *Cytotherapy* **2022**, *24* (6), 567–576.
- (3) Gill, J.; Gorlick, R. Advancing Therapy for Osteosarcoma. *Nat. Rev. Clin. Oncol.* **2021**, *18* (10), 609–624.
- (4) Harrison, D. J.; Geller, D. S.; Gill, J. D.; Lewis, V. O.; Gorlick, R. Current and Future Therapeutic Approaches for Osteosarcoma. *Expert Rev. Anticancer Ther.* **2018**, *18* (1), 39–50.
- (5) Paoluzzi, L.; Cacavio, A.; Ghesani, M.; Karambelkar, A.; Rapkiewicz, A.; Weber, J.; Rosen, G. Response to Anti-PD1 Therapy with Nivolumab in Metastatic Sarcomas. *Clin. Sarcoma Res.* **2016**, *24* (6), 24.
- (6) Stockwell, B. R.; Friedmann Angeli, J. P.; Bayir, H.; Bush, A. I.; Conrad, M.; Dixon, S. J.; Fulda, S.; Gascón, S.; Hatzios, S. K.; Kagan, V. E.; Noel, K.; Jiang, X.; Linkermann, A.; Murphy, M. E.; Overholtzer, M.; Oyagi, A.; Pagnussat, G. C.; Park, J.; Ran, Q.; Rosenfeld, C. S.; Salnikow, K.; Tang, D.; Torti, F. M.; Torti, S. V.; Toyokuni, S.; Woerpel, K. A.; Zhang, D. D. Ferroptosis: A Regulated Cell Death

Nexus Linking Metabolism, Redox Biology, and Disease. *Cell* **2017**, *171* (2), 273–285.

(7) Dixon, S. J.; Stockwell, B. R. The Role of Iron and Reactive Oxygen Species in Cell Death. *Nat. Chem. Biol.* **2014**, *10* (1), 9–17.

(8) Song, R.; Li, T.; Ye, J.; Sun, F.; Hou, B.; Saeed, M.; Gao, J.; Wang, Y.; Zhu, Q.; Xu, Z.; Yu, H. Acidity-Activatable Dynamic Nanoparticles Boosting Ferroptotic Cell Death for Immunotherapy of Cancer. *Adv. Mater.* **2021**, *33* (31), No. e2101155.

(9) Xie, S.; Sun, W.; Zhang, C.; Dong, B.; Yang, J.; Hou, M.; Xiong, L.; Cai, B.; Liu, X.; Xue, W. Metabolic Control by Heat Stress Determining Cell Fate to Ferroptosis for Effective Cancer Therapy. *ACS Nano* **2021**, *15* (4), 7179–7194.

(10) Zanganeh, S.; Hutter, G.; Spitzer, R.; Lenkov, O.; Mahmoudi, M.; Shaw, A.; Pajarinen, J. S.; Nejadnik, H.; Goodman, S.; Moseley, M.; Coussens, L. M.; Daldrop-Link, H. E. Iron Oxide Nanoparticles Inhibit Tumor Growth by Inducing Pro-Inflammatory Macrophage Polarization in Tumour Tissues. *Nat. Nanotechnol.* **2016**, *11* (11), 986–994.

(11) Qian, X.; Zhang, J.; Gu, Z.; Chen, Y. Nanocatalysts-Augmented Fenton Chemical Reaction for Nanocatalytic Tumor Therapy. *Biomaterials* **2019**, *211*, 1–13.

(12) Zhang, F.; Li, F.; Lu, G. H.; Nie, W.; Zhang, L.; Lv, Y.; Bao, W.; Gao, X.; Wei, W.; Pu, K.; Xie, H. Y. Engineering Magnetosomes for Ferroptosis/Immunomodulation Synergism in Cancer. *ACS Nano* **2019**, *13* (5), 5662–5673.

(13) Zhu, W.; Mei, J.; Zhang, X.; Zhou, J.; Xu, D.; Su, Z.; Fang, S.; Wang, J.; Zhang, X.; Zhu, C. Photothermal Nanozyme-Based Microneedle Patch against Refractory Bacterial Biofilm Infection via Iron-Actuated Janus Ion Therapy. *Adv. Mater.* **2022**, *34* (51), No. e2207961.

(14) Khan, J. A.; Mandal, T. K.; Das, T. K.; Singh, Y.; Pillai, B.; Maiti, S. Magnetite (Fe<sub>3</sub>O<sub>4</sub>) Nanocrystals Affect the Expression of Genes Involved in the TGF-β Signalling Pathway. *Mol. Biosyst.* **2011**, *7* (5), 1481–1486.

(15) Rojo de la Vega, M.; Chapman, E.; Zhang, D. D. NRF2 and the Hallmarks of Cancer. *Cancer Cell* **2018**, *34* (1), 21–43.

(16) Zhang, L.; Wang, J. L.; Ba, X. X.; Hua, S. Y.; Jiang, P.; Jiang, F. L.; Liu, Y. Multifunction in One Molecule: Mitochondrial Imaging and Photothermal & Photodynamic Cytotoxicity of Fast-Response Near-Infrared Fluorescent Probes with Aggregation-Induced Emission Characteristics. *ACS Appl. Mater. Interfaces* **2021**, *13* (7), 7945–7954.

(17) Chugh, V.; Vijaya Krishna, K.; Pandit, A. Cell Membrane-Coated Mimics: A Methodological Approach for Fabrication, Characterization for Therapeutic Applications, and Challenges for Clinical Translation. *ACS Nano* **2021**, *15* (11), 17080–17123.

(18) Rao, L.; Tian, R.; Chen, X. Cell-Membrane-Mimicking Nanodecoys against Infectious Diseases. *ACS Nano* **2020**, *14* (3), 2569–2574.

(19) Liu, L.; Bai, X.; Martikainen, M. V.; Kärllund, A.; Roponen, M.; Xu, W.; Hu, G.; Tasciotti, E.; Lehto, V. P. Cell Membrane Coating Integrity Affects the Internalization Mechanism of Biomimetic Nanoparticles. *Nat. Commun.* **2021**, *12* (1), 5726.

(20) Dai, J.; Wu, M.; Wang, Q.; Ding, S.; Dong, X.; Xue, L.; Zhu, Q.; Zhou, J.; Xia, F.; Wang, S.; Hong, Y. Red Blood Cell Membrane-Camouflaged Nanoparticles Loaded with AIEgen and Poly(I: C) for Enhanced Tumor Photodynamic-Immunotherapy. *Natl. Sci. Rev.* **2021**, *8* (6), nwab039.

(21) Dai, J.; Chen, Z.; Wang, S.; Xia, F.; Lou, X. Erythrocyte Membrane-Camouflaged Nanoparticles as Effective and Biocompatible Platform: Either Autologous or Allogeneic Erythrocyte-derived. *Mater. Today Bio* **2022**, *15*, 100279.

(22) Xiong, J.; Wu, M.; Chen, J.; Liu, Y.; Chen, Y.; Fan, G.; Liu, Y.; Cheng, J.; Wang, Z.; Wang, S.; Liu, Y.; Zhang, W. Cancer-Erythrocyte Hybrid Membrane-Camouflaged Magnetic Nanoparticles with Enhanced Photothermal-Immunotherapy for Ovarian Cancer. *ACS Nano* **2021**, *15* (12), 19756–19770.

(23) Jana, D.; He, B.; Chen, Y.; Liu, J.; Zhao, Y. A Defect-Engineered Nanozyme for Targeted NIR-II Photothermal Immunotherapy of Cancer. *Adv. Mater.* **2022**, No. e2206401.

- (24) Xu, C.; Jiang, Y.; Han, Y.; Pu, K.; Zhang, R. A Polymer Multicellular Nanoengager for Synergistic NIR-II Photothermal Immunotherapy. *Adv. Mater.* **2021**, *33* (14), No. e2008061.
- (25) Liu, W.; Zou, M.; Liu, T.; Zeng, J.; Li, X.; Yu, W.; Li, C.; Ye, J.; Song, W.; Feng, J.; Zhang, X. Expandable Immunotherapeutic Nanoplatfoms Engineered from Cytomembranes of Hybrid Cells Derived from Cancer and Dendritic Cells. *Adv. Mater.* **2019**, *31* (18), 1900499.
- (26) Liu, Z.; Zhang, J.; Liu, H.; Shen, H.; Meng, N.; Qi, X.; Ding, K.; Song, J.; Fu, R.; Ding, D.; Feng, G. BSA-AIE Nanoparticles with Boosted ROS Generation for Immunogenic Cell Death Immunotherapy of Multiple Myeloma. *Adv. Mater.* **2022**, *35*, No. e2208692.
- (27) Galluzzi, L.; Buqué, A.; Kepp, O.; Zitvogel, L.; Kroemer, G. Immunogenic Cell Death in Cancer and Infectious Disease. *Nat. Rev. Immunol.* **2017**, *17* (2), 97–111.
- (28) Wang, D.; Dong, H.; Li, M.; Cao, Y.; Yang, F.; Zhang, K.; Dai, W.; Wang, C.; Zhang, X. Erythrocyte-Cancer Hybrid Membrane Camouflaged Hollow Copper Sulfide Nanoparticles for Prolonged Circulation Life and Homotypic-Targeting Photothermal/Chemotherapy of Melanoma. *ACS Nano* **2018**, *12* (6), 5241–5252.
- (29) Fucikova, J.; Kepp, O.; Kasikova, L.; Petroni, G.; Yamazaki, T.; Liu, P.; Zhao, L.; Spisek, R.; Kroemer, G.; Galluzzi, L. Detection of Immunogenic Cell Death and Its Relevance for Cancer Therapy. *Cell Death Dis.* **2020**, *11* (11), 1013.
- (30) Yang, Y.; Wang, Y.; Guo, L.; Gao, W.; Tang, T. L.; Yan, M. Interaction between Macrophages and Ferroptosis. *Cell Death Dis.* **2022**, *13* (4), 355.
- (31) Obeid, M.; Tesniere, A.; Ghiringhelli, F.; Fimia, G. M.; Apetoh, L.; Perfettini, J. L.; Castedo, M.; Mignot, G.; Panaretakis, T.; Casares, N.; Métivier, D.; Larochette, N.; van Endert, P.; Ciccosanti, F.; Piantoni, M.; Zitvogel, L.; Kroemer, G. Calreticulin Exposure Dictates the Immunogenicity of Cancer Cell Death. *Nat. Med.* **2007**, *13* (1), 54–61.
- (32) Apetoh, L.; Ghiringhelli, F.; Tesniere, A.; Obeid, M.; Ortiz, C.; Criollo, A.; Mignot, G.; Maiuri, M. C.; Ullrich, E.; Saulnier, P.; Yang, H.; Amigorena, S.; Ryffel, B.; Barrat, F. J.; Saftig, P.; Levi, F.; Lidereau, R.; Nogue, C.; Mira, J. P.; Chompret, A.; Joulin, V.; Clavel-Chapelon, F.; Bourhis, J.; André, F.; Delaloge, S.; Tursz, T.; Kroemer, G.; Zitvogel, L. Toll-like Receptor 4-Dependent Contribution of the Immune System to Anticancer Chemotherapy and Radiotherapy. *Nat. Med.* **2007**, *13* (9), 1050–1059.
- (33) Garg, A. D.; Krysko, D. V.; Vandenabeele, P.; Agostinis, P. Extracellular ATP and P<sub>2</sub>X<sub>7</sub> Receptor Exert Context-Specific Immunogenic Effects after Immunogenic Cancer Cell Death. *Cell Death Dis.* **2016**, *7* (2), No. e2097.
- (34) Krysko, O.; Love Aaes, T.; Bachert, C.; Vandenabeele, P.; Krysko, D. V. Many Faces of DAMPs in Cancer Therapy. *Cell Death Dis.* **2013**, *4* (5), No. e631.
- (35) Zhao, C.; Cheng, Y.; Huang, P.; Wang, C.; Wang, W.; Wang, M.; Shan, W.; Deng, H. X-Ray Guided in Situ Genetic Engineering of Macrophage for Sustained Cancer Immunotherapy. *Adv. Mater.* **2022**, *35*, No. e2208059.
- (36) Huang, C.; Lin, B.; Chen, C.; Wang, H.; Lin, X.; Liu, J.; Ren, Q.; Tao, J.; Zhao, P.; Xu, Y. Synergistic Reinforcing of Immunogenic Cell Death and Transforming Tumor-Associated Macrophages Via a Multifunctional Cascade Bioreactor for Optimizing Cancer Immunotherapy. *Adv. Mater.* **2022**, *34*, No. e2207593.
- (37) Gu, Z.; Liu, T.; Liu, C.; Yang, Y.; Tang, J.; Song, H.; Wang, Y.; Yang, Y.; Yu, C. Ferroptosis-Strengthened Metabolic and Inflammatory Regulation of Tumor-Associated Macrophages Provokes Potent Tumoricidal Activities. *Nano Lett.* **2021**, *21* (15), 6471–6479.
- (38) Dehaini, D.; Wei, X.; Fang, R. H.; Masson, S.; Angsantikul, P.; Luk, B. T.; Zhang, Y.; Ying, M.; Jiang, Y.; Kroll, A. V.; Gao, W.; Zhang, L. Erythrocyte-Platelet Hybrid Membrane Coating for Enhanced Nanoparticle Functionalization. *Adv. Mater.* **2017**, *29* (16), 1606209.
- (39) Yang, R.; Ouyang, Z.; Guo, H.; Qu, J.; Xia, J.; Shen, M.; Shi, X. Microfluidic Synthesis of Intelligent Nanoclusters of Ultrasmall Iron Oxide Nanoparticles with Improved Tumor Microenvironment Regulation for Dynamic MR Imaging-Guided Tumor Photothermo-Chemo-Chemodynamic Therapy. *Nano Today* **2022**, *46*, 101615.
- (40) Hu, C.-M. J.; Zhang, L.; Aryal, S.; Cheung, C.; Fang, R. H.; Zhang, L. Erythrocyte Membrane-Camouflaged Polymeric Nanoparticles as a Biomimetic Delivery Platform. *Proc. Natl. Acad. Sci.* **2011**, *108* (27), 10980–10985.
- (41) Tang, W.; Zhen, Z.; Wang, M.; Wang, H.; Chuang, Y. J.; Zhang, W.; Wang, G. D.; Todd, T.; Cowger, T.; Chen, H.; Liu, L.; Li, Z.; Xie, J. Red Blood Cell-Facilitated Photodynamic Therapy for Cancer Treatment. *Adv. Funct. Mater.* **2016**, *26* (11), 1757–1768.
- (42) Xu, L.; Sun, Z.; Wei, X.; Tan, H.; Kong, P.; Li, Z.; Yang, Q.; Dai, E.; Li, J. The Inhibition of MARK2 Suppresses Cisplatin Resistance of Osteosarcoma Stem Cells by Regulating DNA Damage and Repair. *J. Bone Oncol.* **2020**, *23*, 100290.
- (43) Pu, Y.; Zhao, F.; Wang, H.; Cai, W.; Gao, J.; Li, Y.; Cai, S. MiR-34a-5p Promotes the Multi-Drug Resistance of Osteosarcoma by Targeting the CD117 Gene. *Oncotarget* **2016**, *7* (19), 28420.
- (44) Shen, Z.; Song, J.; Yung, B. C.; Zhou, Z.; Wu, A.; Chen, X. Emerging Strategies of Cancer Therapy Based on Ferroptosis. *Adv. Mater.* **2018**, *30* (12), 1704007.
- (45) Miotto, G.; Rossetto, M.; Di Paolo, M. L.; Orian, L.; Venerando, R.; Roveri, A.; Vučković, A. M.; Bosello Travain, V.; Zaccarin, M.; Zennaro, L.; Maiorino, M.; Toppo, S.; Ursini, F.; Cozza, G. Insight into the Mechanism of Ferroptosis Inhibition by Ferrostatin-1. *Redox Biol.* **2020**, *28*, 101328.
- (46) Ba, T.; Zhao, D.; Chen, Y.; Zeng, C.; Zhang, C.; Niu, S.; Dai, H. L-Citrulline Supplementation Restrains Ferritinophagy-Mediated Ferroptosis to Alleviate Iron Overload-Induced Thymus Oxidative Damage and Immune Dysfunction. *Nutrients* **2022**, *14* (21), 4549.
- (47) Roh, J. L.; Kim, E. H.; Jang, H.; Shin, D. Nrf2 Inhibition Reverses the Resistance of Cisplatin-Resistant Head and Neck Cancer Cells to Artesunate-induced Ferroptosis. *Redox Biol.* **2017**, *11*, 254–262.
- (48) Sun, X.; Ou, Z.; Chen, R.; Niu, X.; Chen, D.; Kang, R.; Tang, D. Activation of the p62-Keap1-NRF2 Pathway Protects against Ferroptosis in Hepatocellular Carcinoma Cells. *Hepatology* **2016**, *63* (1), 173–184.
- (49) Turubanova, V. D.; Balalaeva, I. V.; Mishchenko, T. A.; Catanzaro, E.; Alzeibak, R.; Peskova, N. N.; Efimova, I.; Bachert, C.; Mitroshina, E. V.; Krysko, O.; Vedunova, M. V.; Krysko, D. V. Immunogenic Cell Death Induced by A New Photodynamic Therapy Based on Photosens and Photodithazine. *J. Immunother. Cancer* **2019**, *7* (1), 350.
- (50) Laidlaw, B. J.; Craft, J. E.; Kaech, S. M. The Multifaceted Role of CD4(+) T Cells in CD8(+) T Cell Memory. *Nat. Rev. Immunol.* **2016**, *16* (2), 102–111.
- (51) Alemi, F.; Malakoti, F.; Vaghari-Tabari, M.; Soleimanpour, J.; Shabestani, N.; Sadigh, A. R.; Khelghati, N.; Asemi, Z.; Ahmadi, Y.; Yousefi, B. DNA Damage Response Signaling Pathways as Important Targets for Combination Therapy and Chemotherapy Sensitization in Osteosarcoma. *J. Cell Physiol.* **2022**, *237* (5), 2374–2386.
- (52) Sadoughi, F.; Maleki Dana, P.; Asemi, Z.; Yousefi, B. DNA Damage Response and Repair in Osteosarcoma: Defects, Regulation and Therapeutic Implications. *DNA Repair* **2021**, *102*, 103105.
- (53) Jackson, S. P.; Bartek, J. The DNA-Damage Response in Human Biology and Disease. *Nature* **2009**, *461* (7267), 1071–1078.
- (54) Sun, X.; Wang, Y.; Ji, K.; Liu, Y.; Kong, Y.; Nie, S.; Li, N.; Hao, J.; Xie, Y.; Xu, C.; Du, L.; Liu, Q. NRF2 Preserves Genomic Integrity by Facilitating ATR Activation and G2 Cell Cycle Arrest. *Nucleic Acids Res.* **2020**, *48* (16), 9109–9123.
- (55) Mavrogatou, E.; Angelopoulou, M.; Rizou, S. V.; Pratsinis, H.; Gorgoulis, V. G.; Kletsas, D. Activation of the JNKs/ATM-p53 Axis Is Indispensable for the Cytoprotection of Dermal Fibroblasts Exposed to UVB Radiation. *Cell Death Dis.* **2022**, *13* (7), 647.
- (56) Anuranjani, Bala, M. Concerted Action of Nrf2-ARE Pathway, MRN Complex, HMGB1 and Inflammatory Cytokines - Implication in Modification of Radiation Damage. *Redox Biol.* **2014**, *2*, 832–846.
- (57) Cuadrado, M.; Martinez-Pastor, B.; Murga, M.; Toledo, L. I.; Gutierrez-Martinez, P.; Lopez, E.; Fernandez-Capetillo, O. ATM

Regulates ATR Chromatin Loading in Response to DNA Double-Strand Breaks. *J. Exp. Med.* **2006**, *203* (2), 297–303.

(58) Yu, Z.; Vogel, G.; Coulombe, Y.; Dubeau, D.; Spehalski, E.; Hébert, J.; Ferguson, D. O.; Masson, J. Y.; Richard, S. The MRE11 GAR Motif Regulates DNA Double-Strand Break Processing and ATR Activation. *Cell Res.* **2012**, *22* (2), 305–320.

(59) Smith, J.; Mun Tho, L.; Xu, N.; A. Gillespie, D. The ATM-Chk2 and ATR-Chk1 Pathways in DNA Damage Signaling and Cancer. *Adv. Cancer Res.* **2010**, *108*, 73–112.

(60) Sun, S.; Zeng, H. Size-Controlled Synthesis of Magnetite Nanoparticles. *J. Am. Chem. Soc.* **2002**, *124* (28), 8204–8205.

(61) Zeng, J.; Jing, L.; Hou, Y.; Jiao, M.; Qiao, R.; Jia, Q.; Liu, C.; Fang, F.; Lei, H.; Gao, M. Anchoring Group Effects of Surface Ligands on Magnetic Properties of Fe<sub>3</sub>O<sub>4</sub> Nanoparticles: Towards High Performance MRI Contrast Agents. *Adv. Mater.* **2014**, *26* (17), 2694.